Pax2a regulates angiogenesis to facilitate mmp2-dependent basement membrane remodeling of the optic fissure.

Megan L. Weaver[1], Piedade. W. P[1], Meshram, N.N[1] and J.K. Famulski[1].

1. Department of Biology, University of Kentucky

Key Words: Optic fissure, coloboma, pax2, hyaloid vasculature, anti-angiogenesis, mmp2

ABSTRACT:

Vertebrate retinal development requires timely and precise fusion of the optic fissure (OF). Recent studies have suggested hyaloid vasculature to be involved in optic fissure fusion. In order to examine this link, we analyzed OF fusion and hyaloid vasculogenesis in the zebrafish pax2a^{noi} mutant line. We determined that OF basement membrane (BM) remodeling, normally preceded by F-actin accumulation is mis-regulated in pax2a$^{-/-}$ embryos. Comparing transcriptomic profiles of pax2a$^{-/-}$ and wildtype eyes we discovered a novel connection between regulation of angiogenesis and fusion. Pax2a$^{-/-}$ eyes exhibited a significant reduction of *talin1* expression, a regulator of hyaloid vasculature, in addition to increased expression of an anti-angiogenic protease, *adamts1*. Using 3D and live imaging we observed reduced OF hyaloid vascularization in pax2a$^{-/-}$ embryos. Additionally, pharmacological inhibition of VEGF signaling or *adamts1* mRNA overexpression phenocopied the pax2a$^{-/-}$ vasculature, F-actin and BM remodeling phenotypes. Finally, we show that hyaloid vasculature expresses *mmp2* which is necessary for remodeling the fissure BM. Taken together we propose a pax2a driven mechanism that restricts anti-angiogenic activity of adamts1 enabling hyaloid vasculature invasion of the OF and delivery of the BM remodeler mmp2.

59 **INTRODUCTION:**

60 Ocular development is a highly conserved process amongst vertebrate species.
61 Assembly of the hemispherical, retinal structure from an initially flat sheet of cells
62 requires many complex morphogenetic movements. One such morphogenetic
63 movement involves the invagination of the optic vesicle which results in a fissure
64 forming at the ventral region of the developing retina. This fissure, known as the choroid
65 or optic fissure (OF), enables hyaloid vasculature cell migration into the developing
66 retina and subsequent establishment of the hyaloid vasculature. Hyaloid vasculature is
67 a temporary circulatory system required for ocular development, and in most cases will
68 degenerate once mature blood vessels begin to grow (1-4). As soon as the hyaloid
69 vasculature has been established, the two opposing retinal epithelial sheets of the optic
70 fissure will undergo fusion. Thereby, they encase the ganglion cell axons localized in
71 the optic stalk and complete retinal morphogenesis. Failure of optic fissure fusion leads
72 to a congenital blinding disorder known as coloboma (5-7). Coloboma is a prevalent
73 cause of pediatric blindness, accounting for approximately 10% of cases worldwide (6,
74 8). This makes it one of the leading causes of pediatric blindness. Coloboma is a
75 spectrum disorder presenting unilaterally or bilaterally and ranging in severity from
76 minor visual impairment, to complete blindness in the affected eye (9). This spectrum of
77 severity is associated with the location and degree to which the choroid fissure was able
78 to fuse and the severity of subsequent loss of ganglion cell axons (7).
79

80 Coloboma has been studied for many decades in many different species. Work
81 over this time has led to a general outline of the signaling and morphogenetic pathways
82 required for proper optic fissure formation and fusion (recently reviewed in (10)). In
83 particular, opposing action of bone morphogenetic protein (BMP) and sonic hedgehog
84 (Shh) signaling establishing the dorsal-ventral pattern of the optic vesicle and ensuring
85 proper expression of optic stalk and OF regulators pax2, vax1 and vax2 (11, 12).
86 However, the actual molecular mechanisms driving optic fissure fusion remains largely
87 unknown. The process of epithelial tissue fusion is not unique to the eye and occurs
88 throughout development, encompassing neural tube closure, palatal shelf formation and
89 eyelid development (13). Epithelial fusion has been studied for over a century, and is

90 known to involve transcriptional regulation, cell signaling pathways and morphogen
91 gradients (14, 15). The actin cytoskeleton is thought to be a crucial component of the
92 machinery driving epithelial fusion in many tissues (16). The importance of the actin
93 cytoskeleton during epithelial fusion involves lamellipodial and filopodial projections
94 between the two opposing epithelia. These help to “zipper” the cells together to form a
95 single continuous sheet. When lamellipodial and filopodial projections are precluded,
96 epithelial fusion often fails (17). Lamellipodia and filopodia have been observed during
97 OF fusion almost 3 decades ago (18-20). However, the functional and regulatory
98 mechanisms behind these projections remain unknown. Another cellular mechanism
99 known to be directly involved in epithelial fusion is the remodeling of the basement
100 membrane (BM). During epithelial fusion, the BM acts as a physical barrier restricting
101 the establishment of cell-cell contacts, which must be removed in order to complete
102 fusion. Recent work from several labs, working on different species, has characterized
103 progressive removal of the BM during OF fusion (21-24). However, the molecular
104 mechanisms facilitating this process, in particular BM remodeling, also remain largely
105 unknown. It was recently suggested that hyaloid vasculature cells migrating through the
106 OF could potentially signal or facilitate BM remodeling (22). Hyaloid vasculature
107 nourishes the developing retina and lens while connecting to the choroid vasculature for
108 proper blood flow (3). Hyaloid vasculogenesis takes advantage of an open optic fissure
109 so that vasculature cells can migrate into the developing optic cup. Once optic fissure
110 fusion is completed, hyaloid vasculature is fully established. James *et al.* 2016, showed
111 that mutations in zebrafish *talin1*, an actin cytoskeleton scaffolding protein known to be
112 required for endothelial cell migration (25), result in OF fusion defects. Theirs, and
113 previous studies also indicated that *cloche* mutants, which lack all early hyaloid
114 vasculature, have delayed basement membrane breakdown in the region of the choroid
115 fissure (22, 26). Since the hyaloid vasculature requires an open fissure to complete
116 establishment of its network, it has been proposed that migrating hyaloid vasculature
117 cells may regulate the timing of fissure fusion. This mechanism could potentially involve
118 vasculature-mediated activation of the fusion machinery within the retinal rim cells, or
119 direct supply of molecular factors, such as matrix proteases (27). In additional support
120 of this hypothesis, recent optic cup transplantation experiments in zebrafish embryos

121 confirm that in the absence of hyaloid vasculature, ectopic retinal OFs fail to initiate
122 fusion (28). Hence, there is a clear link between OF fusion and hyaloid vasculature.
123
124 In our current study, we have undertaken a detailed analysis of zebrafish OF
125 fusion comparing WT and the pax2a$^{-/-}$ coloboma model (29). In particular, we have
126 characterized the timing of BM remodeling, cytoskeletal responses, morphological
127 apposition and hyaloid vascularization. Using transcriptomic analysis to compare WT
128 and pax2a$^{-/-}$ eyes we discovered mis-regulation in angiogenic signaling, resulting in
129 decreased OF hyaloid vascularization and OF fusion failure. In particular we found that
130 pax2a$^{-/-}$ embryos exhibit a decrease in *talin1* expression coupled with increased
131 expression of an anti-angiogenic protease, *a disintegrin and metalloproteinase with*
132 *thrombospondin motifs 1 (adamts1*), (30, 31). Modulation of vascularization via
133 pharmacological inhibition of VEGF signaling or overexpression of adamts1 both
134 phenocopied the pax2a$^{-/-}$ hyaloid vasculature and coloboma phenotypes.
135 Mechanistically, we also show that hyaloid vasculature is a source of mmp2, mmp14a
136 and mmp14b and that mmp2 activity is necessary for OF BM remodeling. Taken
137 together, we propose a novel pathway for the regulation of OF fusion where pax2a
138 mediates proper expression of *adamts1* in order to facilitate hyaloid vasculature
139 recruitment to the OF and subsequent vasculature supplied mmp2-dependent BM
140 remodeling.
141
142
143 **RESULTS:**
144 **Optic fissure basement membrane remodeling is preceded by F-actin**
145 **accumulation.**
146 Several recent studies have undertaken a detailed time course to map out the
147 exact timing of optic fissure fusion in numerous species, including zebrafish (21-24).
148 Overall, in zebrafish, the data point to ~32-36hpf as the time of OF fusion initiation, as
149 observed by BM remodeling. To decipher the molecular mechanisms regulating OF
150 fusion we also performed a detailed time course analysis of OF BM remodeling using
151 laminin immunohistochemistry (IHC) and additionally analyzed F-actin. Our goal was to

152 determine whether changes in F-actin levels in the OF were correlative with fusion.
153 James *et al*, 2016 had recently suggested that infiltrating vasculature endothelial cells
154 migrating through the fissure could be a source of signal for fissure fusion. In fact, they
155 have shown that interactions between vasculature and the fissure resulted in an
156 increase of F-actin (22). As such, we performed whole mount IHC for laminin deposition
157 in embryos starting at 24hpf. We sampled every 4 hours up to 48hpf and then at 56 and
158 72hpf (Fig 1A). To analyze the progression of the fusion process, we quantified the
159 laminin signal within the OF from 3D confocal scans. Regions of the BM outside the OF
160 and juxtaposed to the developing lens were used to normalize the laminin signal (Fig
161 S1A). We quantified distal, medial and proximal regions of the fissure (Fig S1B,C).
162 When comparing results from the three regions we did not observe significant
163 differences in the distribution of laminin or F-actin. Going forward we focused on
164 quantifying laminin signal in the central proximal region (medial) of the fissure (Fig S1B).
165 This region has been previously shown to represent the site of fusion initiation and is
166 easily identified in 24-72hpf embryos. In agreement with recent studies in zebrafish, we
167 found that OF fusion initiates at ~32-36hpf and does so in a central region of the fissure,
168 subsequently proceeding proximally and distally (Fig 1B). By 48hpf, we observed most
169 of the laminin signal was removed from the OF, and by 72hpf, little to no laminin
170 persists in the region (Fig 1A, B).
171 To track F-actin levels during fusion we stained the laminin labeled embryos with
172 phalloidin and quantified the signal within the fissure. To normalize phalloidin staining
173 intensity we used an interior region of the retina (Fig S1A). Our analysis revealed an
174 increase in OF associated F-actin signal between 24-32hpf, preceding the time that BM
175 remodeling is initiated (Fig 1A,B). We also noticed a second increase in F-actin around
176 44hpf, a time of active fusion (Fig 1C). The observed increase of F-actin signal
177 correlates with a) the timing of hyaloid vasculature migration (24-32hpf) into the fissure
178 and b) the expected timing of actin protrusions involved in epithelial fusion (36-48hpf).
179 When measuring distance between the fusing lobes of the retina we observed
180 apposition to complete around 36-40hpf (Fig S2). Taken together, we conclude that
181 both apposition and BM remodeling are preceded by an increase of F-actin within the
182 OF.

183

184 **Optic fissure fusion mechanics are disrupted upon loss of pax2a function.**

185 In order to test our theory that an increase in F-actin is involved in the initiation of
186 OF fusion we compared our findings to an established model of coloboma, the pax2a^{noi}
187 line (29). Pax2 is required for OF fusion in several model systems and has been
188 documented in human coloboma cases (32-34). The noi mutation is predicted to result
189 in a loss of pax2a function due to a premature stop codon at position 198 (35).
190 Originally characterized for their no-isthmus phenotype, pax2a$^{noi/noi}$ embryos (referred to
191 as pax2a$^{-/-}$ from this point on) elicit a fully penetrant unfused OF. Unfortunately,
192 homozygous mutants are not viable and do not enable the study of coloboma at juvenile
193 or adult stages. We hypothesized that examining the molecular events leading to OF
194 fusion in the pax2a^{noi} system would inform us whether these events are functionally
195 important. Similar to our WT study, we examined apposition, laminin and F-actin levels
196 throughout the time of OF fusion (Fig 2A, Fig S1C). In stark contrast to WT, pax2a$^{-/-}$
197 embryos did not exhibit a significant decrease in laminin signal between 32-48hpf. In
198 fact, as expected, laminin appears to be largely retained in the OF of pax2a$^{-/-}$ embryos
199 up to 72hpf (Fig 2B). Previous studies in pax2a null mice had indicated failure of BM
200 remodeling and retention of laminin (34, 36, 37). While there is a moderate decrease in
201 laminin signal in pax2a$^{-/-}$ embryos from 32-36hpf, this result is significantly different from
202 WT. IHC images clearly show that laminin persists in the fissure up to and including
203 72hpf (Fig 2A). When examining OF F-actin levels in pax2a$^{-/-}$ embryos we did not detect
204 the expected increase between 24 and 32hpf (Fig 2C). We observed F-actin levels
205 fluctuating between 36 and 44hpf and finally dropping to WT amounts by 48hpf. Similar
206 results were also observed when quantifying distal and proximal regions of the fissure
207 (Fig S1D). Our data therefore suggest that the absence of OF F-actin accumulation
208 between 24 and 32hpf, correlates with failure to initiate fusion. Lastly, when examining
209 retinal lobe distance in pax2a$^{-/-}$ embryos we did not observe any significant defects in
210 the timing of apposition (Fig S2). Taken together, we conclude that in the absence of
211 pax2a F-actin fails to accumulate in the OF and this correlates with the failure to
212 remodel the BM. Based on our analysis of apposition, we also conclude that pax2a
213 does not regulate morphogenetic movements of the retinal lobes. In summary, we

214 propose that accumulation of F-actin is necessary for the initiation of OF BM
215 remodeling. We therefore next sought to investigate the mechanism of OF F-actin
216 accumulation.
217
218 **Pax2a retinal transcriptomic profile during optic fissure fusion.**
219 Although pax2 has been studied in many systems, there are currently no obvious
220 transcriptional targets of pax2 that would directly point to mechanistic regulation of OF
221 fusion. In an effort to understand the absence of OF BM remodeling and mis-regulation
222 of F-actin observed in pax2a$^{-/-}$ embryos we compared whole eye transcriptomic profiles
223 between WT and pax2a$^{-/-}$ embryos. Eyes from 48hpf WT and pax2a$^{-/-}$ embryos were
224 isolated and total RNA was subsequently purified and sequenced using Illumina
225 sequencing. 48hpf was chosen for our experimental time point as pax2a$^{-/-}$ embryos are
226 easily phenotyped at this age thanks to observable heart malformations. When
227 comparing three replicates for WT and pax2a$^{-/-}$ embryos using RSEM software, we
228 detected 1215 transcripts significantly upregulated (>95% confidence interval) and 1202
229 transcripts significantly downregulated (Fig 3A and 3D). Gene ontology analysis
230 indicated a wide spread of biological function being affected, including cytoskeletal
231 signaling, adhesion and developmental processes (Fig 3B, E). In fact, the distribution of
232 biological function between up and downregulated genes was highly similar (Fig 3B, D).
233 A list of the top 20 up and down regulated genes is outlined in Figure 3C and F. Results
234 of all the statistically significant up and downregulated genes identified in our assay are
235 presented as supplementary data (Table 1 and Table 2).
236 When examining our list of downregulated targets, one, *talin1* (tln1), stood out in
237 particular. Not only was *tln1* one of the most downregulated targets (~200 fold
238 decrease) it was also recently shown to be necessary for the migration of hyaloid
239 vasculature cells into the OF and subsequent fusion (22). As such, we next sought to
240 investigate the relationship between pax2a, tln1, vasculogenesis and optic fissure fusion
241 mechanics.
242
243 **Loss of pax2a function leads to reduced hyaloid vasculature within the optic**
244 **fissure.**

245 To validate our RNAseq data, we performed wholemount *in situ* hybridization
246 (WISH) for *tln1* comparing WT siblings to pax2a$^{-/-}$ mutant embryos. WT expression of
247 *tln1* was observed in the optic fissure between 28 and 48hpf coinciding with pax2a
248 expression (Fig 4A, Fig S3). In pax2a$^{-/-}$ embryos, OF *tln1* expression appears
249 significantly reduced compared to WT while retaining similar expression in periocular
250 regions (Fig 4A). *Tln1* expression is also reduced in the mid brain-hind brain boundary,
251 another region of strong *pax2a* expression (Fig 4A, S3A). Our WISH data was further
252 supported by qPCR results showing a significant decrase in *tln1* expression at 32hpf
253 (Fig 4B). To determine whether the reduction of *tln1* expression in pax2a$^{-/-}$ embryos had
254 functional consequences on hyaloid vasculogenesis we examined pax2a$^{-/-}$
255 Tg[kdrl:mCherry] embryos. Using 3D *in vivo* time-lapse confocal microscopy we
256 recorded migration of mCherry expressing cells through the OF from 24 to 30hpf (Fig
257 4B, Movie 1). At 24hpf, both WT and pax2a$^{-/-}$ embryos contain mCherry expressing cells
258 within the fissure. However, over the next six hours of imaging it is apparent that pax2a^{-}
259 $^{/-}$ embryos have significantly fewer mCherry expressing cells pass through the OF (Fig
260 4C, Movie 1). To quantify this effect, we fixed WT and pax2a$^{-/-}$ Tg[kdrl:mCherry]
261 embryos at 24, 32, 36 and 48hpf, collected 3D confocal stacks and counted the number
262 of mCherry positive cells found within the OF (Fig 4D). The data indicate that in pax2a$^{-/-}$
263 embryos there is a significant reduction in the number of mCherry expressing cells at
264 both 32 and 36hpf (Fig 4E). Furthermore, using 3D rendering, we noted that in 48hpf
265 pax2a$^{-/-}$ embryos the hyaloid vasculature established in the back of the lens is reduced
266 in size and lacks proper connections to the newly forming choroidal and superficial
267 vasculature systems (Movie 2-3). Overall, our data indicate that pax2a$^{-/-}$ embryos exhibit
268 decreased expression of *tln1* and impaired hyaloid vascularization of the optic fissure.
269

270 **<u>Inhibition of VEGF signaling impairs optic fissure fusion mechanics.</u>**

271 Based on our discovery of impaired OF hyaloid vasculature in pax2a$^{-/-}$ embryos,
272 we next examined whether this phenomenon is associated with failure of optic fissure
273 fusion. Hence, we turned our attention to vascular endothelial growth factor (VEGF)
274 signaling. VEGF, the ligand for vascular endothelial growth factor receptor (VEGFR), is
275 a prime candidate for regulating the migration and proliferation of hyaloid vasculature

276 cells. In support of this notion, when examining expression patterns for VEGF ligands,
277 vegfaa and ab, ba, c and d, we found *vegfaa, ab* and *c* to be expressed in the retina and
278 periocular regions (Fig S4A). To inhibit VEGF signaling, we took advantage of the
279 dorsomorphin derivative DMH4, which has been shown in zebrafish to selectively inhibit
280 VEGF signaling independent from BMP (38). Based on published working
281 concentrations, we conducted a dose response to examine DHM4 effects on hyaloid
282 vasculature using Tg[kdrl:mCherry] as a readout (38). Treatment of embryos from 12-
283 24hpf, ranging from 1-100μM, resulted in a dose dependent reduction of mCherry signal
284 in the developing retina (Fig S4B). We decided to use the 100μM concentration for
285 subsequent experiments as this concentration was able to completely inhibit
286 vascularization of the retina up to 72hpf without any significant impact on overall embryo
287 health (Fig 5A, S4C). Embryos were treated starting at 12hpf and examined for fissure
288 fusion status via whole mount laminin IHC at 24, 32, 36, 48, 56 and 72hpf (Fig 5B). 3D
289 confocal imaging revealed a persistence of laminin signal within the fissure up and
290 including 72hpf in all embryos examined (Fig 5B). Measurement of the laminin signal
291 generated very similar results to what we observed in pax2a$^{-/-}$ embryos (Fig 5C). This is
292 highlighted by retention of laminin signal at 48hpf and persistence of laminin in 100%
293 (n=49) of embryos treated up to 72hpf (Fig 5B-C). In addition to laminin, we also imaged
294 and quantified OF F-actin levels during the treatment (Fig 5B). Similar to pax2a$^{-/-}$
295 embryos DMH4 treatment prevented the accumulation of OF F-actin between 24-32hpf
296 (Fig 5D). This was in contrast to DMSO treated embryos which exhibited the
297 accumulation of F-actin in the fissure between 24-32hpf like wildtype embryos. DMH4
298 treatment did not affect the size of the retina nor the apposition of retinal lobes (Fig S2).
299 Lastly, we also observed a significant decrease of *tln1,* but not *pax2a,* expression in
300 DMH4 treated embryos (Fig S4E,F). This suggests that *tln1* is likely expressed by the
301 vasculature cells within the OF. Based on these findings, we conclude that inhibition of
302 VEGF signaling results in failure of F-actin accumulation and basement membrane
303 breakdown, presumably due to the absence of hayloid vasculature cells in the OF.
304
305 **Anti-angiogenic protease *adamts1* is upregulated in OF of pax2a mutant embryos.**

306 Having established a connection between pax2a function and recruitment of
307 hyaloid vasculature cells into the optic fissure, we next sought to examine the
308 mechanism behind it. We therefore re-examined our transcriptomic comparison of WT
309 and pax2a$^{-/-}$ eyes, with a focus on angiogenic regulation. This new examination
310 revealed misexpression of *a disintegrin and metalloproteinase with thrombospondin*
311 *motifs 1* (adamts1), a secreted protease known to be involved in regulating VEGF
312 signaling (39). Being a member of the ADAMTS family, adamts1 contains three
313 thrombospondin motifs enabling it to directly bind and sequester VEGF (31).
314 Furthermore, the protease activity of adamts1 has bene shown to target
315 thrombospondin 1 and 2 for cleavage, ultimately liberating their active forms which bind
316 to and block VEGF from binding the VEGF receptor (30). Our RNAseq data indicated
317 that *adamts1* expression was upregulated almost two-fold in pax2a$^{-/-}$ eyes (table 1). This
318 would suggest that the expression of *adamts1*, and therefore its anti-angiogenic activity,
319 is normally kept in check by pax2a. Pax2a has not been reported to harbor
320 transcriptionally repressive function, so this may involve an indirect mechanism. To
321 confirm our RNAseq results we performed WISH, examining *adamts1* expression at 28
322 and 36hpf. In agreement with our transcriptomic analysis, we observed an upregulation
323 in *adamts1* in the ventral region of pax2a$^{-/-}$ eyes, specifically surrounding the optic
324 fissure (Fig 6A). A statistically significant increase in *adamts1* expression was also
325 confirmed using qPCR (Fig 6B). To test whether upregulation of *adamts1* expression
326 would have direct effects on hyaloid vascularization and optic fissure fusion we injected
327 Tg[*kdrl*:mCherry] embryos with *adamts1* mRNA. We subsequently examined hyaloid
328 vasculature using 3D confocal imaging between 24-48hpf. Injection of *adamts1* mRNA
329 resulted in a significant decrease in the number of *kdrl*:mCherry cells found within the
330 optic fissure (Fig 6B, C, Movie 5). The observed decrease mirrored the results from
331 pax2a$^{-/-}$ embryos (Fig 6C). Our findings therefore suggest that *adamts1* expression
332 needs to be tightly regulated in order to ensure proper vascularization of the retina,
333 including the OF. Furthermore, the observed up-regulation of *adamts1* expression in
334 pax2a$^{-/-}$ embryos may explain the resulting OF hyaloid vasculature deficiency.
335
336 **Overexpression of *adamts1* inhibits optic fissure fusion mechanics.**

337 Having mimicked the vasculature phenotype of pax2a mutants by over
338 expressing *adamts1*, we next determined whether it had any effects on OF fusion. To
339 do so, we performed whole mount laminin and F-actin staining in *adamts1* mRNA
340 injected embryos at 24, 32, 36, and 48hpf (Fig 7A). Confocal imaging of the fissure
341 indicated that *adamts1* mRNA injection also phenocopied pax2a$^{-/-}$ associated
342 persistence of laminin and therefore failure of optic fissure fusion. Quantified levels of
343 laminin persisting at 48hpf was similar to pax2a$^{-/-}$ embryos (Fig 7B). Similar to pax2a$^{-/-}$
344 and DMH4 treated embryos, we again noted a lack F-actin accumulation between 24-
345 32hpf in *adamts1* overexpressing embryos (Fig 7C). As was observed with pax2a$^{-/-}$,
346 timing for apposition of the lobes was not affected in adamts1 overexpressing embryos
347 (Fig S2). Taken together, our data suggest that maintaining proper levels of *adamts1*
348 expression is necessary to enable VEGF signaling and subsequent recruitment of
349 hyaloid vasculature required for initiation of OF BM remodeling.
350
351 **Hyaloid vasculature is the source of mmp2 necessary for OF BM remodeling.**
352 The above data confirm and support a model where hyaloid vasculature drives or
353 initiates the OF fusion process. However, a missing key to this model is the mechanism
354 by which vasculature cells induce fissure fusion. James *et al*, along with others, have
355 suggested vasculature cells may be a source of BM remodeling enzymes, such as
356 matrix metaloproteases (mmp). To investigate this further, we used WISH to examine
357 mmp expression within the OF between 24-48hpf. Our data indicated that *mmp2, 14a*
358 and *14b* were expressed within the fissure between 28-36hpf (Fig S5 and Famulski lab
359 unpublished data). Mmp2 had recently been associated with OF fusion in the mouse
360 while evidence from an mmp2 metalloproteinase activity probe in zebrafish indicated
361 mmp2 activity is present in the developing eye and likely OF (40, 41). mmp14 is an
362 activator of mmp2 and its co-expression with mmp2 within the fissure suggests mmp2 is
363 in fact active (42, 43). To test whether mmp2 fits within our model we assayed *mmp2,*
364 *mmp14a and mmp14b* expression in pax2a$^{-/-}$ and DMH4 treated embryos. In both
365 cases, OF expression of *mmp2, mmp14a and mmp14b* was reduced as observed by
366 WISH and confirmed by qPCR (Fig 8A, B). This suggested that all three are expressed
367 by the hyaloid vasculature cells. To confirm this, we performed 2 color WISH for *mmp2*

368 and *kdrl*. Confocal imaging verified that *mmp2* expression is co-localized with that of
369 *kdrl* within the OF (Fig 8C). Conversely, when performing 2 color WISH for *mmp2* and
370 *rorB*, a retina specific probe, we did not detect co-localization of the signals. We
371 therefore conclude that the source of mmp2, 14a and 14b enzymes in the OF are
372 hyaloid vasculature cells. Finally, to determine whether mmp2 activity is necessary for
373 OF fusion we treated embryos with ARP101, an mmp2 specific inhibitor previously
374 shown to be effective in zebrafish (44). Treating embryos from 24-48hpf inhibited OF
375 BM remodeling in a dose dependent manner (Fig 8D,E, S6). When compared to DMSO,
376 embryos treated with 20μM ARP101 either completely or partially retain their OF BM up
377 to 48hpf. Mmp2 activity is therefore necessary for BM remodeling in the OF. To
378 determine when mmp2 activity is required we began the ARP101 treatment between
379 24-32hpf and assayed BM status at 48hpf (Fig 8F). Treatments started later than 30hpf
380 had little to no effect on OF BM remodeling, indicating that mmp2 activity is required
381 between ~24-30hpf (Fig 8F). This finding also correlates with the observed timing of
382 *mmp2* expression in the OF (Fig S5). However, because we cannot determine exactly
383 how quickly ARP101 inhibits enzymatic activity in our assay, active mmp2 may persist
384 in the OF longer than 30hpf.
385
386 **DISCUSSION:**
387 Studies of optic fissure fusion dating back several decades have been suggesting a
388 direct connection between the fusion process and hyaloid vasculature found within the
389 fissure. In fact, this hypothesis has been recently strengthened by data showing that a
390 reduction of hyaloid vasculature in the fissure, or removal of optic vesicles from sources
391 of vasculature inhibits or significantly delays fusion (22, 28). In our study, we have
392 characterized a pax2a driven mechanism that ensures proper vascularization of the OF
393 by restricting anti-angiogenic activity of adamts1 to enable hyaloid vasculature invasion
394 of the OF and delivery of BM remodelers mmp2, 14a and 14b. In conclusion, our
395 findings further validate the notion that hyaloid vasculature is an active component of
396 the machinery driving OF fusion.
397

398 Several recent reports, including this one, have comprehensively characterized optic
399 fissure fusion timing (21-24). Work from zebrafish, mice and chick all point to an orderly
400 progression involving: **1)** retinal growth and cellular rearrangement leading to nasal and
401 temporal retinal lobe apposition, **2)** invasion of the fissure by endothelial and neural
402 crest cells forming the hyaloid vasculature system, **3)** cellular signaling, either between
403 retinal rim cells or between rim cells and the migrating vasculature cells, **4)** remodeling
404 or removal of the basement membrane to enable physical connection of the rim cells
405 and subsequent formation of a continuous retinal epithelial sheet via re-polarization and
406 cell-cell adhesion. Step 1 has been nicely characterized in a few recent publications
407 outlining the flow of retinal cells and morphological formation of the fissure (45-47). For
408 step 2, several reports have carefully characterized the formation of the hyaloid
409 vasculature system, including migration of hyaloid vasculature precursor cells into the
410 fissure as soon as it forms (1-3). Importantly, perturbation of this process, or removal of
411 the developing eye from its source, has been shown to lead to fissure fusion failure (22,
412 28). To date, steps 3 and 4 are the least understood. Recent work from our lab has
413 characterized the composition of core BM components within the fissure (23).
414 Additionally, work from other labs has identified several molecular components
415 associated with cell-cell adhesion and epithelial sheet fusion to function within the
416 fissure, including α-catenin, n-cadherin, and netrin (22, 24, 48-51). However, the timing
417 and the molecular mechanism organizing and regulating these components remains
418 uncharacterized. Finally, the elephant in the room has always been the identity of the
419 BM remodeling mechanism. To date, only adamts16 has been functionally examined in
420 context of fissure fusion, mmp2 activity was detected during mouse OF fusion and
421 mmp23bb was implicated in the fusion process from transcriptomic data (41, 50, 52).
422 While attempting to address the mechanistic aspects of steps 3 and 4 using the
423 pax2a^{noi} model we first uncovered a relationship between F-actin and BM remodeling.
424 Work by *James et al. 2016* suggested that F-actin accumulation may be indicative of
425 hyaloid cell interaction with retinal rim cells. During our detailed time course analysis,
426 we discovered that BM remodeling is in fact preceded by an increase in F-actin signal
427 within the OF (Fig 1). When assayed in pax2a$^{-/-}$ embryos the F-actin accumulation is
428 absent while the hyaloid vasculature in the OF is also diminished. The timing of F-actin

429 accumulation coincides with the active migration of hyaloid vasculature cells through the
430 fissure (Fig 4). Furthermore, we show pharmacologically, via VEGF inhibition, that
431 hyaloid vasculature is necessary for the accumulation of F-actin and OF BM
432 remodeling. Transcriptionally, we show that the decrease in hayloid vasculature in
433 pax2a$^{-/-}$ embryos coincides with a significant decrease in *tln1* expression. Tln1 is a key
434 regulator of endothelial cell migration, recently shown to be directly involved in OF
435 fusion (22). In fact, loss of tln1 function has been previously shown to decrease in
436 fissure associated vasculature and inhibit OF BM remodeling (22). We also show a
437 significant decrease in *tln1* expression upon VEGF inhibition (DMH4 treatment),
438 suggesting that *tln1* expression within the OF is associated with hayloid vasculature.
439 Talin1 is known to be a direct link between the actin cytoskeleton and the BM via
440 integrin (53, 54), and has been associated with the formation of adhesion junctions (55,
441 56). One could therefore hypothesize several different models for its role in optic fissure
442 fusion. We predict that tln1 is regulating the ability of hayloid vasculature cells to migrate
443 properly through the OF, however we cannot rule out the possibility that tln1 directly
444 participates in the OF fusion process. The absence of tln1 expression is most likely a
445 correlation to the decrease of hayloid vasculature cells within the fissure of pax2a$^{-/-}$
446 embryos. Our transcriptomic analysis was performed using whole eye tissue, which
447 would have included the hayloid vasculature. As such, the decrease in *tln1* expression
448 is likely indicative of decreased numbers of hayloid vasculature cells which require *tln1*
449 expression for proper migration into the fissure and or proliferation.
450
451 Our study strongly supports the notion that vasculature plays an integral part in OF
452 fusion. As such, modulation of angiogenesis represents a potential mechanism to
453 ensure proper vascularization of the OF. In our transcriptomic comparison of WT and
454 pax2a mutants we did in fact discover a connection to angiogenesis. In the absence of
455 pax2a function we observed an upregulation of *adamts1*. Examining *adamts1*
456 expression in the eye further confirmed an upregulation of expression in the ventral
457 regions pax2a$^{-/-}$ retinas. Encoding 3 thrombospondin (thsb) motifs able to directly bind
458 and sequester VEGF, in addition to targeting thsb1 and 2 for cleavage into their active
459 VEGF inhibiting form, adamts1 is well known for it's anti-angiogenic function in cancer,

460 aortic and renal biology (57). In our study, we show that upregulating adamts1
461 expression reduces the number of hyaloid vasculature cells in the OF. Up regulation of
462 adamts1 also prevents the accumulation of F-actin and subsequent BM remodeling.
463 Taken together we propose that the reduction in hayloid vasculature observed in
464 pax2a$^{-/-}$ embryos likely stems from an upregulation of adamts1 leading to suppressed
465 VEGF signaling and therefore limited vascularization of the OF.
466
467 The last aspect of our proposed model pertains to the mechanism of OF BM
468 remodeling. It had been suggested over the years that vasculature may be the source of
469 BM remodeling activity during OF fusion. To that end, we have discovered that *mmp2*,
470 *mmp14a* and *mmp14b* are all expressed within the hayloid vasculature during OF
471 fusion. In fact, timing of their expression matches precisely with the initiation of BM
472 remodeling. When we examine pax2a mutants or inhibit hayloid vasculature completely
473 we no longer detect expression of either of these mmps. Furthermore, using ARP101, a
474 specific mmp2 inhibitor, we show that mmp2 activity is necessary for OF BM remodeling
475 and this activity is specifically required between 26-32hpf. Mmp2 has been implicated
476 in OF fusion previously. Mouse studies have shown mmp2 expression within
477 macrophages residing in the OF. Furthermore, recent examination of mmp2 activity,
478 using a reporter construct, indicates that mmp2 is active in the eye and likely the OF
479 (40). Mmp14 is a known to activate mmp2 activity by cleaving the inhibitory pro-peptide
480 of mmp2. As such, co-expression of mmp2 and 14 is further indicative of mmp2 playing
481 a functional role in OF BM remodeling.
482 To date, the only BM remodeling enzyme to be associated with OF fusion is
483 adamts16. Loss of adamts16 function in zebrafish, via morpholino, led to a coloboma
484 like phenotype which the authors credited to the inability to degrade laminin in the
485 fissure (52). We have not been able to reproduce adamts16 expression within the
486 fissure. Recent studies in mice, zebrafish and chick have compared expression in OF
487 cells pre, during and post fusion (24, 50, 58, 59). Surprisingly, none of these studies
488 identified any obvious candidates for carrying out BM remodeling, including mmp2 and
489 mmp14. However, it remains possible that the OF tissue examined lacked the hayloid
490 vasculature and therefore prevented the identification of mmp2 and mmp14 as

candidates. Lastly, expression of *mmp2, 14a* and *14b* is transient in the fissure which may have contributed to their OF expression being missed by other groups. Our data indicate mmp2 activity is necessary for BM remodeling of the OF, but does not rule out a role for additional proteases. There may be several proteases involved, such as adamts16, mmp2 and others yet inhibition of just one could trigger failure of the remodeling process and lead to fissure fusion failure. Continuing studies into matrix protease activity will be needed to fully characterize the remodeling mechanisms during OF fusion.

In conclusion, we present a new model for the mechanism of OF BM remodeling where pax2a restricts expression of *adamts1* in the ventral retina to enable hayloid vasculature invasion of the OF. Once in the fissure, vasculature cells express *mmp2, 14a* and *14b* to initiate BM remodeling. As soon as fusion begins, vasculature becomes restricted from the fissure and ultimately the two retinal lobes fuse. Our model aligns with the molecular events observed in the fissure, including accumulation of F-actin at the time of vasculature migration through the fissure (24-28hpf), expression of mmps (26-36hpf) and subsequent BM remodeling (32-48hpf). For future studies it will be important to understand how pax2a regulates *adamts1* expression and to examine whether mutations in *adamts1*, *mmp2* or *mmp14* are potential markers for coloboma.

511 **FIGURE LEGENDS:**

512

513 Figure 1: **An increase in F-actin dynamics precedes laminin remodeling during**
514 **optic fissure fusion.**
515 **A)** Whole mount immunohistochemistry was used to simultaneously visualize F-actin
516 (red) and laminin (green) during optic fissure fusion, 24-72hpf. Central-proximal sections
517 obtained using confocal imaging were collected and quantified. Scale bar = 50um. **B)**
518 Quantification of laminin signal intensity within the optic fissure, normalized to regions of
519 laminin staining juxtaposed to the lens. Relative pixel intensities are displayed. The
520 green dotted line depicts the trend in laminin intensity over time. ANOVA $p<0.0001$. **C)**
521 Quantification of F-actin intensity (phalloidin staining) within the optic fissure, normalized
522 to regions of F-actin signal within the lobe of the retina. Relative pixel intensities are
523 displayed. The blue dotted line represents the trend in F-actin intensity over time.
524 ANOVA $p<0.0001$.

525

526 Figure 2: **Pax2 mutant embryos lack F-actin activity increase and laminin**
527 **remodeling within the optic fissure.**
528 **A)** Whole mount Immunohistochemistry was used to simultaneously visualize F-actin
529 (red) and laminin (green) during optic fissure fusion, 24-72hpf, in pax2$^{-/-}$ embryos.
530 Central-proximal regions of the optic fissure are displayed. Scale bar = 50um **B)**
531 Quantification of laminin signal intensity within the central-proximal region of the optic
532 fissure, normalized to regions of laminin staining juxtaposed to the lens. Relative pixel
533 intensities are displayed. ANOVA $p<0.0001$. **C)** Quantification of F-actin intensity
534 (phalloidin staining) within the central-proximal region of the optic fissure, normalized to
535 regions of F-actin signal within the lobe of the retina. Relative pixel intensities are
536 displayed. The blue dotted line represents the trend of F-actin intensity observed in WT
537 embryos. ANOVA $p<0.0001$.

538

539 Figure 3: **Retinal transcriptomic comparison between WT and pax2a$^{-/-}$.**
540 **A)** Heat map representing transcripts found to be significantly down regulated in pax2a$^{-/-}$
541 embryos. **B)** Gene ontology for pax2a$^{-/-}$ downregulated transcripts. **C)** Top 20

542 downregulated transcripts are outlined in order of fold change. **D)** Heat map
543 representing transcripts found to be significantly upregulated in pax2a$^{-/-}$ embryos. **E)**
544 Gene ontology for pax2a$^{-/-}$ upregulated transcripts. **F)** Top 20 upregulated transcripts
545 are outlined in order of fold change.
546
547 Figure 4: **Pax2a is necessary for *tln1* expression and recruitment of vasculature**
548 **into the optic fissure.**
549 **A)** Wholemount in situ hybridization comparing *tln1* expression between WT and
550 pax2a$^{-/-}$ embryos at 28 and 32hpf. *tln1* signal within the optic fissure (yellow arrowhead)
551 appears reduced in Pax2a$^{-/-}$ embryos (red *). **B)** qPCR analysis of *tln1* expression in WT
552 and pax2a-/- embryos at 32hpf confirms a reduction in *tln1* expression. **C)** *In vivo* 4D
553 confocal imaging of Tg[kdrl:mCherry] WT or pax2a$^{-/-}$ embryos. Time lapse series
554 depicting the region of the optic fissure (dotted white lines) and mCherry positive
555 vasculature endothelial cells migrating through the fissure from 24-29hpf. Scale bar =
556 10um. **D)** Comparison of WT and pax2a$^{-/-}$ vascularization during optic fissure fusion, 24-
557 48hpf. 3D reconstructions of whole mount Tg[kdrl:mCherry] (red) WT or pax2a$^{-/-}$
558 embryos with DAPI (blue) stained DNA. Scale bar = 50μm. **E)** Quantification of the
559 number of mCherry positive cells from 3D confocal stacks within the region of the optic
560 fissure. Individual embryo results are depicted. ANOVA $p<0.0001$.
561
562 Figure 5: **Inhibiting angiogenesis prevents optic fissure fusion.**
563 **A)** 3D confocal imaging of Tg[kdrl:mCherry] (red) embryos treated with DMSO or 100μM
564 DMH4 between 24-72hpf. DNA was stained with DAPI (blue). Scale bar = 50μm. DMH4
565 treatment results in the absence of hyaloid vasculature the fissure and retina. **B)** Whole
566 mount Immunohistochemistry was used to simultaneously visualize F-actin (red) and
567 laminin (green) in DMH4 treated embryos from 24-72hpf. Central-proximal regions of
568 the optic fissure are displayed. Treatment with DMH4 results in retention of laminin and
569 optic fissure fusion failure. Scale bar = 50μm. **C)** Quantification of laminin signal
570 intensity within the central-proximal region of the optic fissure, normalized to regions of
571 laminin staining juxtaposed to the lens. Relative pixel intensities are displayed. ANOVA
572 $p<0.0001$. **D)** Quantification of F-actin signal intensity (phalloidin staining) within the

573 central-proximal region of the optic fissure, normalized to regions of F-actin signal within
574 the lobe of the retina. Relative pixel intensities are displayed. A blue dotted line
575 represents the WT trend in F-actin intensity. ANOVA p<0.0001.
576
577 Figure 6: **Adamts1 inhibits retinal vascularization.**
578 **A)** Wholemount in situ hybridization comparing *adamts1* expression between WT and
579 pax2a$^{-/-}$ embryos at 28 and 32hpf. *adamts1* signal within the optic fissure (yellow
580 arrowhead) is appears increased in Pax2a$^{-/-}$ embryos (red *). **B)** qPCR analysis
581 confirms an increase in *adamts1* expression in pax2a-/- embryos. **C)** Comparison of WT
582 and adamts1 mRNA injected embryo vascularization during optic fissure fusion, 24-
583 48hpf. 3D reconstructions of whole mount Tg[kdrl:mCherry] (red) WT or adamts1 mRNA
584 injected embryos with DNA stained by DAPI (blue). Scale bar = 50μm. **D)** Quantification
585 of mCherry positive cells from 3D confocal stacks within the region of the optic fissure.
586 Individual embryo results are depicted. * p<0.001, ANOVA p<0.0001.
587
588 Figure 7: ***Adamts1* misregulation leads to failure of optic fissure fusion.**
589 **A)** Whole mount Immunohistochemistry was used to simultaneously visualize F-actin
590 (red) and laminin (green) during optic fissure fusion, 24-72hpf in adamts1 mRNA
591 injected embryos. Central-proximal regions of the optic fissure are displayed. Scale bar
592 = 50μm. **B)** Quantification of laminin signal intensity within the central-proximal regions
593 of the optic fissure, normalized to regions of laminin staining juxtaposed to the lens.
594 Relative pixel intensities are displayed. ANOVA p<0.0001. **C)** Quantification of F-actin
595 signal intensity (phalloidin staining) within the central-proximal regions of the optic
596 fissure, normalized to regions of F-actin signal within the lobe of the retina. Relative
597 pixel intensities are displayed. A blue dotted line represents the WT trend in F-actin
598 intensity over time. ANOVA p<0.0001.
599
600 Figure 8: **Hyaloid vasculature is the source of mmp2 activity required for optic**
601 **fissure BM remodeling.**
602 **A)** Wholemount in situ hybridization comparing *mmp2, mmp14a* and *mmp14b*
603 expression in WT vs pax2a$^{-/-}$ and DMSO vs DMH4 treated embryos at 32hpf. *Mmp2,*

604 *14a and 14b* signal within the optic fissure (yellow arrowhead) appears decreased in
605 pax2a$^{-/-}$ and DMH4 treated embryos. **B)** qPCR analysis confirms a decrease in
606 expression of *mmp2, 14a* and *14b* in both pax2a$^{-/-}$ and DMH4 treated embryos. **C)** Two
607 color wholemount in situ hybridization simultaneously examining *mmp2* and *kdrl*, or
608 *mmp2* and *rorB* expression at 32hpf. DNA was stained with DAPI. Scale bar = 50μm.
609 Clear overlap of signal is observed for *mmp2* and *kdrl*, but not *mmp2* and *rorB*. **D)**
610 Whole mount Immunohistochemistry was used to visualize laminin (red) in ARP101
611 treated Tg[*rx3*:GFP] embryos at 48hpf. Central-proximal regions of the optic fissure are
612 displayed. **E)** Quantification of 48hpf ARP101 treated embryos for fissure fusion
613 (absence of laminin signal), partial fusion (partial retention of laminin) or failure to fuse
614 (retention of laminin throughout the fissure). n= 41 (10mM), 38 (15mM), 42 (20mM)
615 ANOVA $p<0.0001$. **F)** Quantification of 48hpf ARP101 treated embryos for fissure
616 fusion, partial fusion or failure to fuse after various treatment initiation times from 24-
617 32hpf. n= 42 (24-48hpf), 29 (26-48hpf), 29 (28-48hpf), 23 (30-48hpf), 37 (32-48hpf).
618 ANOVA $p<0.0001$.
619
620
621
622
623
624

625 **Supplemental Material**

626

627 Figure S1: **Optic Fissure quantification**

628 **A**) Graphical representation of the region of OF analyzed using confocal microscopy. **B**)
629 Sample image depicting regions of the OF (1), laminin normalization (2) and F-actin
630 normalization (3) used for signal intensity quantification**. C)** Quantification of laminin and
631 F-actin signal intensity in wild type embryos within the distal, medial and proximal
632 regions of the optic fissure, normalized to regions of laminin staining juxtaposed to the
633 lens and F-actin signal within the lobe of the retina. Relative pixel intensities are
634 displayed. ANOVA $p<0.0001$. **D)** Quantification of laminin and F-actin signal intensity in
635 pax2a$^{-/-}$ embryos within the distal, medial and proximal regions of the optic fissure,
636 normalized to regions of laminin staining juxtaposed to the lens and F-actin signal within
637 the lobe of the retina. Relative pixel intensities are displayed. ANOVA $p<0.0001$.

638

639 Figure S2: **Optic Fissure apposition measurements.**

640 Measurements of the distance between retinal lobes (apposition) in WT, pax2a$^{-/-}$, DMH4
641 treated or ADAMTS1 mRNA injected embryos at 48hpf. Measurements were made
642 using laminin staining as reference for edges of retinal lobes. Distance was measured
643 as pixels.

644

645 Figure S3: ***pax2a* and *tln1* expression during development**

646 **A**) Whole mount in situ hybridization of *pax2a* probe at 24, 48, 54 and 72hpf. Lateral
647 (top) and ventral (bottom) images depicting optic fissure expression are shown. Pax2a
648 expression persists in the fissure up to 54hpf. **B**) Whole mount in situ hybridization of
649 *tln1* probe at 24, 48, 54 and 72hpf. Lateral (top) and ventral (bottom) images depicting
650 optic fissure expression are shown. *tln1* expression is detected in the optic fissure from
651 24-48hpf (yellow arrowheads).

652

653 Figure S4: **DMH4 dose response**

654 **A)** Whole mount in situ hybridization of *vegfaa, ab, ba, c* and *d* probes at 32hpf. **B)** 3D
655 reconstructions of 48hpf whole mount Tg[kdrl:mCherry] (red) embryos treated with 1, 5,

656 50 or 100uM DMH4. DNA stained with DAPI (blue). Increasing concentration of DMH4
657 eliminates mCherry expressing cells from the optic fissure and retina. Scale bar =
658 50μm. **C)** Brightfield images of DMSO or DMH4 treated embryos at 24, 48 and 72hpf.
659 **D)** Whole mount in situ hybridization of *pax2a* or *tln1* probe at 32hpf in DMSO or DMH4
660 treated embryos. OF expression is indicated with a yellow arrowhead. DMH4 treatment
661 does not appear to alter *pax2a* expression but eliminates *tln1* expression from the OF.
662 **E)** qPCR results for *tln1* expression in DMH4 treated embryos.
663
664 Figure S5: **Time course of *mmp2, mmp14a* and *mmp14b* ocular expression**
665 Whole mount in situ hybridization of *mmp2, mmp14a, mmp14b* probes at 24, 26, 30 32,
666 34, 36 and 38hpf. *Mmp2* expression is present in the optic fissure from 26-34hpf (yellow
667 arrowheads). *Mmp14a* expression is present in the optic fissure from 32-36hpf(yellow
668 arrowheads). *Mmp14b* expression is present in the optic fissure from 32-36hpf (yellow
669 arrowheads).
670
671 Figure S6: **ARP101 treatment dose response**
672 **A)** Brightfield images of DMSO and ARP treated embryos at 48hpf. Concentrations of
673 ARP101 exceeding 20uM result in toxic effects. **B)** Whole mount Immunohistochemistry
674 was used to visualize laminin (red) in ARP101 treated Tg[*rx3*:GFP] embryos at 48hpf.
675 Central-proximal and distal regions of the optic fissure are displayed.
676
677 Movie 1: WT Tg[kdrl:mCherry] migration within the optic fissure, 24-30hpf
678
679 Movie 2: pax2a$^{-/-}$ Tg[kdrl:mCherry] migration within the optic fissure, 24-30hpf
680
681 Movie 3: 3D rotation of WT Tg[kdrl:mCherry] embryo at 48hpf
682
683 Movie 4: 3D rotation of pax2a$^{-/-}$ Tg[kdrl:mCherry] embryo at 48hpf
684
685 Movie 5: 3D rotation of 48hpf Tg[kdrl:mCherry] embryo injected with ADAMTS1 mRNA
686

687 Movie 6: 3D rotation of 48hpf Tg[kdrl:mCherry] embryo injected with ADAMTS1
688 morpholino
689
690 Table 1: 95th percentile RNA sequencing comparison
691
692 Table 2: Raw data RNA sequencing comparison
693
694 Table 3: Primer sequences
695
696 **MATERIALS AND METHODS:**
697
698 Zebrafish and embryo maintenance
699 Zebrafish were maintained using husbandry procedures approved by University of
700 Kentucky IACUC committee. Embryos were kept at 28.5°C in E3 embryo media. AB and
701 TL strains were used as wild-type, Tg[*kdrl*:mCherry] transgenic line was used to
702 visualize retinal vascularization (60), Tg[*rx3*:GFP] was used to visualize retinal cells
703 (61).
704 Pax2^{noi} embryos were a gift from Dr. Gregory-Evans. Genotyping analysis was
705 conducted by amplifying the region of gDNA with the noi mutation using the forward
706 primer: 5'- CTCGCTCTGCCTCCATGATTG3-'and the reverse: 5'-
707 GGCACTGAAAGAGCACAGG -3'. The resultant 460bp amplicon was digested with
708 TaqI (NEB) which would recognize and digest the WT allele sequence but not the
709 mutant allele.
710
711 Immunohistochemistry (IHC)
712 Dechorionated embryos were fixed with 4% PFA in PBS at room temperature for 3h
713 and washed with PBST 4 times for 5 minutes. Embryos were then permeabilized with
714 Proteinase K, 30μg/mL 10 minutes for 24-28hpf, 50μg/mL 15-20 minutes for 32-48hpf
715 and 75μg/mL 20 minutes for 56-72hpf, washed 2 times in PBST for 5 minutes and
716 blocked overnight at 4°C with 10% sheep serum, 0.8% Triton X-100 and 1% BSA in
717 PBS. Primary mouse anti-laminin antibody (ThermoFisher – 1:100) in blocking buffer
718 (1% sheep serum, 1% BSA and 0.8% Triton X-100 in PBS) were incubated overnight at
719 4°C and washed 5 times in PBST for 15 minutes. Secondary antibody, goat anti-rabbit

720 (Alexa Fluor® 488 – Abcam – 1:1000), DAPI 1:1000, and phalloidin (Alexa Fluor® 555 -
721 1:50) were incubated overnight at 4°C in the dark. Tg[*kdrl*:mCherry] embryos were
722 treated with proteinase K as described above and stained with DAPI 1:1000 overnight.
723 The embryos were washed 2 times in PBST for 15 minutes and visualized using a
724 Nikon C2+ confocal microscope equipped with a 40X (1.15NA) water immersion
725 objective. Embryos were embedded in 1.2% low melting point agarose on glass bottom
726 35mm dishes (Fluorodish, World Precision Instruments). Images were captured in steps
727 of 3.5 microns for a total of 31.5 microns using Nikon Elements software. Image
728 adjustment, such as cropping and brightness/contrast was performed using Adobe
729 Photoshop.
730
731 Analysis of Fluorescence signal
732 Fiji software (https://fiji.sc) was used to measure the fluorescence intensity of laminin
733 and phalloidin signal from raw image data. In order to account for variability in staining,
734 normalization values were measured for laminin and actin pixel intensity where an area
735 directly outside of the choroid fissure was measured and a ratio was generated between
736 the two values (Fig S1B). In cases where the fissure edges were farther apart then the
737 size of the box used for analysis, the box was divided into two and used to measure
738 fluorescence intensity on each side of the fissure. Measured values from both boxes
739 was added and then normalized. For Tg[krdl:mCherry], 3D reconstructions of the optic
740 fissure were generated and individual cells were counted (from the opening of the OF
741 through the back of the lens).
742
743 Stats
744 Student's t-test was used to compare individual time points. One-way ANOVA was
745 used to analyze across treatments. Graphs are displayed as mean +/- standard
746 deviation. Analysis was performed using Prism8 graphing software (GraphPad).
747
748 Total RNA Sequencing
749 WT and Pax2$^{-/-}$ embryos were dissected and collected at 48hpf and RNA was
750 extracted from dissected eyes using trizol. Pax2a$^{-/-}$ embryos were phenotyped by

751 distinct heart defects only observed in pax2a$^{-/-}$ embryos, as verified by previous
752 genotyping experiments. Dissected eyes were suspended in 1 mL of trizol and sheared
753 with a 22-gauge needle. Samples were incubated at room temperature for 5 minutes,
754 then 200 μL of chloroform was added and vortexed for 1 minute. Samples were then
755 centrifuged at 12,000 g for 15 minutes at 4℃. Aqueous phase was removed and put into
756 fresh RNAse free tube. 3 μL of Glycoblue was added to samples and vortexed for 5
757 seconds. 500 μL of 100% Isopropanol was then added and vortexed for an additional 10
758 seconds. Samples then were incubated at room temperature for 10 minutes.
759 Subsequently, samples were centrifuged at 12,000 g for 10 minutes at 4℃. Supernatant
760 was removed and 1 mL of 75% EtOH was added and vortexed for 10 seconds. Samples
761 were then centrifuged at 7,500 g for 5 minutes at 4℃. Supernatant was removed and
762 samples then underwent a pulse centrifugation and any remaining supernatant was
763 removed. Samples were air-dried for 7 minutes at room temperature under a fume
764 hood. 20 μL of RNAse free ddH_2O was added to the samples and mixed until pellet
765 dissolved. Finally, samples were incubated at 60℃ for 12 minutes and stored at -80℃.
766 The RNA then underwent a DNase treatment using the DNA-free Kit. 2 μL of 10X
767 DNaseI Buffer, and 1 μL of rDNaseI was added to the entire 20 μL sample. Samples
768 were incubated at 37℃ for 20 minutes, and then 2 μL of DNase Inactivation Reagent
769 was added. Samples were then incubated at room temperature for 2 minutes, mixing
770 samples 3 times. Samples were centrifuged at 10,000 g for 1.5 minutes. Supernatant
771 was then removed and placed into fresh RNase free tube and stored at -80℃.
772 Purified total RNA was sent to Applied Biological Materials Inc. for Illumina
773 sequencing (PE150bp, 30-40 million reads/sample). Bioinformatic analyses were
774 completed using RSEM. Those transcripts which had a greater than 0.95 posterior
775 probability of being differentially expressed were considered significant. Panther
776 (http://pantherdb.org) was used for gene ontology and pie chart generation.
777
778 Whole-mount in situ hybridization (WISH)
779 Whole-mount in situ hybridization was performed as previously described (62). RNA
780 probes were generated using PCR with T7 promoter sequence linkers and
781 subsequently transcribed [DIG or FITC labeled] using T7 polymerase (Roche). Primer

782 sequences are all found in Table 3. Images were captured using a Nikon Digital sight
783 DS-Fi2 camera mounted on a Nikon SZM800 stereo scope using Elements software.
784 Dissected eyes from 24, to 72hpf embryos were mounted in 70% glycerol and imaged
785 under DIC using a Nikon TiE compound microscope equipped with a 20X (0.7NA)
786 objective and Elements software. Image adjustment, such as cropping and
787 brightness/contrast was performed using Adobe Photoshop.
788
789 qPCR analysis
790 32hpf embryos were anesthetized with tricane, tail tips were collected for genotyping
791 and the heads, dissected just posterior of the eyes, were fixed in RNAlater. After
792 genotyping, embryos corresponding to WT and pax2a-/- were pooled, 5-10 embryos,
793 and total RNA isolated using a RNAaqueous kit (Ambion). DMSO and DMH4 treated
794 embryos were harvested in the same fashion absent any genotyping. qPCR was
795 performed as previously described (63).
796
797 2 color fluorescent in situ hybridization
798 Fluorescent whole mount in situ hybridization was performed as previously described
799 (64). Images were collected using a Nikon C2+ confocal microscope with a 20X
800 (0.95NA) objective and images were adjusted for brightness and contrast using Adobe
801 Photoshop.
802
803 Live imaging analysis
804 Live imaging of Tg[kdrl:mCherry] embryos was conducted using a Nikon C2+ confocal
805 microscope equipped with at 20X (0.95NA) water immersion objective. 22hpf embryos
806 were imbedded in 1.1% low gelling agarose in 1-inch glass bottomed Flourodish cell
807 culture dishes (World Precision Instruments) and covered in embryo media, 3-amino
808 benzoic acidethylester (tricaine) to anaesthetize the embryos and 1-phenyl 2-thiourea
809 (PTU) to inhibit pigmentation. Z-stacks 75μm thick with a step size of 2.5μm were
810 captured over the course of 6 hours at 10 minute intervals. The time lapse data were
811 reconstructed in 3D using Elements software. Image adjustment, such as cropping and

812 brightness/contrast was performed using Adobe Photoshop. After imaging, embryos
813 were removed and genotyped.
814
815 Inhibitor treatments
816 Embryos were incubated in embryo media with 5, 25, 50, or 100 μM of DMH-4 (Sigma
817 Life Science) in DMSO starting at 12hpf. Fresh DHM4 containing media was added
818 every 12hpf for timepoints past 24hpf. For ARP101 (Tocris) treatments embryos were
819 dechorionated and treated with 10, 15, 20, 25 or 30μM ARP101 in fish water from 24 to
820 48hpf, unless stated otherwise.
821
822 Cloning and mRNA synthesis.
823 Full coding domain sequences for *adamts1* (NCBI reference sequence
824 XM_021475923.1), were amplified from 24hpf zebrafish cDNA using primers 5'-
825 CTCGAGTCAACAGGGAGTCAGATTGC-3' for *adamts1*, cloned into pGEMT
826 (Promega), digested with AsiSI/XhoI, BamHI/XhoI respectively and subsequently cloned
827 into pCS2+. All constructs were verified by sanger sequencing (Eurofinsgenomics).
828 mRNA was synthesized from linearized pCS2 constructs using SP6 mMessage
829 mMachine kit (Ambion) and purified using YM-50 Microcon columns (Amicon, Millipore).
830
831 Ethics Statement
832 The use of zebrafish in this study was approved by the University of Kentucky IACUC
833 committee, Institutional PHS Assurance #D16-00217 (A3336-01) with a protocol
834 number: 2015-1370.
835
836
837 **ACKNOWLEDGEMENTS:**
838
839 This work for supported by faculty start-up funds provided to JKF from the department
840 of Biology, University of Kentucky. MLW was supported by the Lyman T Johnson
841 scholarship from the University of Kentucky. WPP was supported by Brazilian National
842 Council for Scientific and Technological Development (CNPq) under grant number

843 202970/2014-0. We thank Dr. Jeramiah Smith for assistance with bioinformatic analysis
844 of our RNAseq data and members of the Famulski lab for helpful discussions.
845
846

847 **REFERENCES:**
848

849 1. Hartsock A, Lee C, Arnold V, Gross JM. In vivo analysis of hyaloid vasculature
850 morphogenesis in zebrafish: A role for the lens in maturation and maintenance of the hyaloid.
851 Dev Biol. 2014;394(2):327-39.
852 2. Hashiura T, Kimura E, Fujisawa S, Oikawa S, Nonaka S, Kurosaka D, et al. Live imaging of
853 primary ocular vasculature formation in zebrafish. PLoS One. 2017;12(4):e0176456.
854 3. Kaufman R, Weiss O, Sebbagh M, Ravid R, Gibbs-Bar L, Yaniv K, et al. Development and
855 origins of zebrafish ocular vasculature. BMC Dev Biol. 2015;15:18.
856 4. Yoshikawa Y, Yamada T, Tai-Nagara I, Okabe K, Kitagawa Y, Ema M, et al. Developmental
857 regression of hyaloid vasculature is triggered by neurons. J Exp Med. 2016;213(7):1175-83.
858 5. AS AL, Gregory-Evans CY, Gregory-Evans K. An update on the genetics of ocular
859 coloboma. Hum Genet. 2019.
860 6. Chang L, Blain D, Bertuzzi S, Brooks BP. Uveal coloboma: clinical and basic science
861 update. Curr Opin Ophthalmol. 2006;17(5):447-70.
862 7. Gregory-Evans CY, Williams MJ, Halford S, Gregory-Evans K. Ocular coloboma: a
863 reassessment in the age of molecular neuroscience. J Med Genet. 2004;41(12):881-91.
864 8. Stoll C, Alembik Y, Dott B, Roth MP. Congenital eye malformations in 212,479
865 consecutive births. Ann Genet. 1997;40(2):122-8.
866 9. Huynh N, Brooks BP. Uveal coloboma. JAMA Ophthalmol. 2013;131(10):1274.
867 10. Patel A, Sowden JC. Genes and pathways in optic fissure closure. Semin Cell Dev Biol.
868 2017.
869 11. Take-uchi M, Clarke JD, Wilson SW. Hedgehog signalling maintains the optic stalk-retinal
870 interface through the regulation of Vax gene activity. Development. 2003;130(5):955-68.
871 12. Macdonald R, Wilson SW. Pax proteins and eye development. Curr Opin Neurobiol.
872 1996;6(1):49-56.
873 13. Ray HJ, Niswander L. Mechanisms of tissue fusion during development. Development.
874 2012;139(10):1701-11.
875 14. Hayes P, Solon J. Drosophila dorsal closure: An orchestra of forces to zip shut the
876 embryo. Mech Dev. 2017;144(Pt A):2-10.
877 15. Jacinto A, Martinez-Arias A, Martin P. Mechanisms of epithelial fusion and repair. Nat
878 Cell Biol. 2001;3(5):E117-23.
879 16. Vasioukhin V, Bauer C, Yin M, Fuchs E. Directed actin polymerization is the driving force
880 for epithelial cell-cell adhesion. Cell. 2000;100(2):209-19.
881 17. Gumbiner BM. Cell adhesion: the molecular basis of tissue architecture and
882 morphogenesis. Cell. 1996;84(3):345-57.
883 18. Hero I. The optic fissure in the normal and microphthalmic mouse. Exp Eye Res.
884 1989;49(2):229-39.
885 19. Hero I. Optic fissure closure in the normal cinnamon mouse. An ultrastructural study.
886 Invest Ophthalmol Vis Sci. 1990;31(1):197-216.
887 20. Geeraets R. An electron microscopic study of the closure of the optic fissure in the
888 golden hamster. Am J Anat. 1976;145(4):411-31.
889 21. Bernstein CS, Anderson MT, Gohel C, Slater K, Gross JM, Agarwala S. The cellular bases
890 of choroid fissure formation and closure. Dev Biol. 2018;440(2):137-51.

891 22. James A, Lee C, Williams AM, Angileri K, Lathrop KL, Gross JM. The hyaloid vasculature
892 facilitates basement membrane breakdown during choroid fissure closure in the zebrafish eye.
893 Dev Biol. 2016;419(2):262-72.
894 23. Carrara N, Weaver M, Piedade WP, Vocking O, Famulski JK. Temporal characterization of
895 optic fissure basement membrane composition suggests nidogen may be an initial target of
896 remodeling. Dev Biol. 2019.
897 24. Hardy H, Prendergast JG, Patel A, Dutta S, Trejo-Reveles V, Kroeger H, et al. Detailed
898 analysis of chick optic fissure closure reveals Netrin-1 as an essential mediator of epithelial
899 fusion. Elife. 2019;8.
900 25. Monkley SJ, Kostourou V, Spence L, Petrich B, Coleman S, Ginsberg MH, et al.
901 Endothelial cell talin1 is essential for embryonic angiogenesis. Dev Biol. 2011;349(2):494-502.
902 26. Dhakal S, Stevens CB, Sebbagh M, Weiss O, Frey RA, Adamson S, et al. Abnormal retinal
903 development in Cloche mutant zebrafish. Dev Dyn. 2015;244(11):1439-55.
904 27. Heissig B, Hattori K, Friedrich M, Rafii S, Werb Z. Angiogenesis: vascular remodeling of
905 the extracellular matrix involves metalloproteinases. Curr Opin Hematol. 2003;10(2):136-41.
906 28. Gestri G, Bazin-Lopez N, Scholes C, Wilson SW. Cell Behaviors during Closure of the
907 Choroid Fissure in the Developing Eye. Front Cell Neurosci. 2018;12:42.
908 29. Macdonald R, Scholes J, Strahle U, Brennan C, Holder N, Brand M, et al. The Pax protein
909 Noi is required for commissural axon pathway formation in the rostral forebrain. Development.
910 1997;124(12):2397-408.
911 30. Lee NV, Sato M, Annis DS, Loo JA, Wu L, Mosher DF, et al. ADAMTS1 mediates the
912 release of antiangiogenic polypeptides from TSP1 and 2. EMBO J. 2006;25(22):5270-83.
913 31. Luque A, Carpizo DR, Iruela-Arispe ML. ADAMTS1/METH1 inhibits endothelial cell
914 proliferation by direct binding and sequestration of VEGF165. J Biol Chem. 2003;278(26):23656-
915 65.
916 32. Sanyanusin P, McNoe LA, Sullivan MJ, Weaver RG, Eccles MR. Mutation of PAX2 in two
917 siblings with renal-coloboma syndrome. Hum Mol Genet. 1995;4(11):2183-4.
918 33. Sanyanusin P, Schimmenti LA, McNoe LA, Ward TA, Pierpont ME, Sullivan MJ, et al.
919 Mutation of the PAX2 gene in a family with optic nerve colobomas, renal anomalies and
920 vesicoureteral reflux. Nat Genet. 1995;9(4):358-64.
921 34. Torres M, Gomez-Pardo E, Gruss P. Pax2 contributes to inner ear patterning and optic
922 nerve trajectory. Development. 1996;122(11):3381-91.
923 35. Brand M, Heisenberg CP, Jiang YJ, Beuchle D, Lun K, Furutani-Seiki M, et al. Mutations in
924 zebrafish genes affecting the formation of the boundary between midbrain and hindbrain.
925 Development. 1996;123:179-90.
926 36. Favor J, Sandulache R, Neuhauser-Klaus A, Pretsch W, Chatterjee B, Senft E, et al. The
927 mouse Pax2(1Neu) mutation is identical to a human PAX2 mutation in a family with renal-
928 coloboma syndrome and results in developmental defects of the brain, ear, eye, and kidney.
929 Proc Natl Acad Sci U S A. 1996;93(24):13870-5.
930 37. Otteson DC, Shelden E, Jones JM, Kameoka J, Hitchcock PF. Pax2 expression and retinal
931 morphogenesis in the normal and Krd mouse. Dev Biol. 1998;193(2):209-24.
932 38. Hao J, Ho JN, Lewis JA, Karim KA, Daniels RN, Gentry PR, et al. In vivo structure-activity
933 relationship study of dorsomorphin analogues identifies selective VEGF and BMP inhibitors. ACS
934 Chem Biol. 2010;5(2):245-53.

935 39. Tan Ide A, Ricciardelli C, Russell DL. The metalloproteinase ADAMTS1: a comprehensive
936 review of its role in tumorigenic and metastatic pathways. Int J Cancer. 2013;133(10):2263-76.
937 40. Jeffrey EJ, Crawford BD. The epitope-mediated MMP activation assay: detection and
938 quantification of the activation of Mmp2 in vivo in the zebrafish embryo. Histochem Cell Biol.
939 2018;149(3):277-86.
940 41. Tsuji N, Matsuura T, Narama I, Yoshiki A, Ozaki K. Macrophage-Associated Gelatinase
941 Degrades Basement Membrane at the Optic Fissure Margins During Normal Ocular
942 Development in Mice. Invest Ophthalmol Vis Sci. 2018;59(3):1368-73.
943 42. Nishida Y, Miyamori H, Thompson EW, Takino T, Endo Y, Sato H. Activation of matrix
944 metalloproteinase-2 (MMP-2) by membrane type 1 matrix metalloproteinase through an
945 artificial receptor for proMMP-2 generates active MMP-2. Cancer Res. 2008;68(21):9096-104.
946 43. Strongin AY, Collier I, Bannikov G, Marmer BL, Grant GA, Goldberg GI. Mechanism of cell
947 surface activation of 72-kDa type IV collagenase. Isolation of the activated form of the
948 membrane metalloprotease. J Biol Chem. 1995;270(10):5331-8.
949 44. Theodore LN, Hagedorn EJ, Cortes M, Natsuhara K, Liu SY, Perlin JR, et al. Distinct Roles
950 for Matrix Metalloproteinases 2 and 9 in Embryonic Hematopoietic Stem Cell Emergence,
951 Migration, and Niche Colonization. Stem Cell Reports. 2017;8(5):1226-41.
952 45. Eckert P, Knickmeyer MD, Schutz L, Wittbrodt J, Heermann S. Morphogenesis and axis
953 specification occur in parallel during optic cup and optic fissure formation, differentially
954 modulated by BMP and Wnt. Open Biol. 2019;9(2):180179.
955 46. Heermann S, Schutz L, Lemke S, Krieglstein K, Wittbrodt J. Eye morphogenesis driven by
956 epithelial flow into the optic cup facilitated by modulation of bone morphogenetic protein.
957 Elife. 2015;4.
958 47. Knickmeyer MD, Mateo JL, Eckert P, Roussa E, Rahhal B, Zuniga A, et al. TGFbeta-
959 facilitated optic fissure fusion and the role of bone morphogenetic protein antagonism. Open
960 Biol. 2018;8(3).
961 48. Chen S, Lewis B, Moran A, Xie T. Cadherin-mediated cell adhesion is critical for the
962 closing of the mouse optic fissure. PLoS One. 2012;7(12):e51705.
963 49. Lahrouchi N, George A, Ratbi I, Schneider R, Elalaoui SC, Moosa S, et al. Homozygous
964 frameshift mutations in FAT1 cause a syndrome characterized by colobomatous-
965 microphthalmia, ptosis, nephropathy and syndactyly. Nat Commun. 2019;10(1):1180.
966 50. Richardson R, Owen N, Toms M, Young RM, Tracey-White D, Moosajee M.
967 Transcriptome profiling of zebrafish optic fissure fusion. Sci Rep. 2019;9(1):1541.
968 51. Smith R, Huang YT, Tian T, Vojtasova D, Mesalles-Naranjo O, Pollard SM, et al. The
969 Transcription Factor Foxg1 Promotes Optic Fissure Closure in the Mouse by Suppressing Wnt8b
970 in the Nasal Optic Stalk. J Neurosci. 2017;37(33):7975-93.
971 52. Cao M, Ouyang J, Guo J, Lin S, Chen S. Metalloproteinase Adamts16 Is Required for
972 Proper Closure of the Optic Fissure. Invest Ophthalmol Vis Sci. 2018;59(3):1167-77.
973 53. Anthis NJ, Wegener KL, Ye F, Kim C, Goult BT, Lowe ED, et al. The structure of an
974 integrin/talin complex reveals the basis of inside-out signal transduction. EMBO J.
975 2009;28(22):3623-32.
976 54. Wegener KL, Partridge AW, Han J, Pickford AR, Liddington RC, Ginsberg MH, et al.
977 Structural basis of integrin activation by talin. Cell. 2007;128(1):171-82.

978 55. Calderwood DA, Campbell ID, Critchley DR. Talins and kindlins: partners in integrin-
979 mediated adhesion. Nat Rev Mol Cell Biol. 2013;14(8):503-17.
980 56. Prout M, Damania Z, Soong J, Fristrom D, Fristrom JW. Autosomal mutations affecting
981 adhesion between wing surfaces in Drosophila melanogaster. Genetics. 1997;146(1):275-85.
982 57. Boerboom D, Lafond JF, Zheng X, Lapointe E, Mittaz L, Boyer A, et al. Partially redundant
983 functions of Adamts1 and Adamts4 in the perinatal development of the renal medulla. Dev Dyn.
984 2011;240(7):1806-14.
985 58. Brown JD, Dutta S, Bharti K, Bonner RF, Munson PJ, Dawid IB, et al. Expression profiling
986 during ocular development identifies 2 Nlz genes with a critical role in optic fissure closure. Proc
987 Natl Acad Sci U S A. 2009;106(5):1462-7.
988 59. Cao M, Ouyang J, Liang H, Guo J, Lin S, Yang S, et al. Regional Gene Expression Profile
989 Comparison Reveals the Unique Transcriptome of the Optic Fissure. Invest Ophthalmol Vis Sci.
990 2018;59(15):5773-84.
991 60. Wang Y, Kaiser MS, Larson JD, Nasevicius A, Clark KJ, Wadman SA, et al. Moesin1 and
992 Ve-cadherin are required in endothelial cells during in vivo tubulogenesis. Development.
993 2010;137(18):3119-28.
994 61. Hocking JC, Famulski JK, Yoon KH, Widen SA, Bernstein CS, Koch S, et al. Morphogenetic
995 defects underlie Superior Coloboma, a newly identified closure disorder of the dorsal eye. PLoS
996 Genet. 2018;14(3):e1007246.
997 62. Holly VL, Widen SA, Famulski JK, Waskiewicz AJ. Sfrp1a and Sfrp5 function as positive
998 regulators of Wnt and BMP signaling during early retinal development. Dev Biol.
999 2014;388(2):192-204.
1000 63. Pereira Piedade W, Veith S, Famulski JK. Ubiquitin-mediated proteasome degradation
1001 regulates optic fissure fusion. Biol Open. 2019;8(6).
1002 64. Lauter G, Soll I, Hauptmann G. Two-color fluorescent in situ hybridization in the
1003 embryonic zebrafish brain using differential detection systems. BMC Dev Biol. 2011;11:43.
1004

Figure 1

A

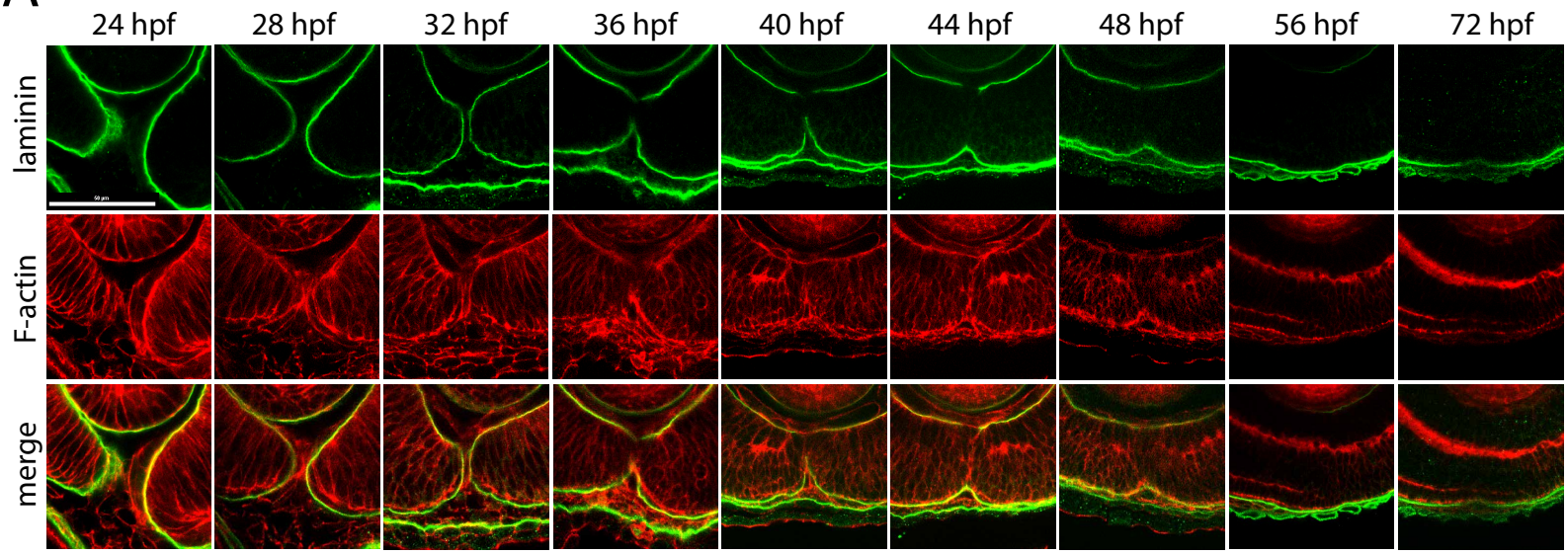
24 hpf
28 hpf
32 hpf
36 hpf
40 hpf
44 hpf
48 hpf
56 hpf
72 hpf
laminin
F-actin
merge

B

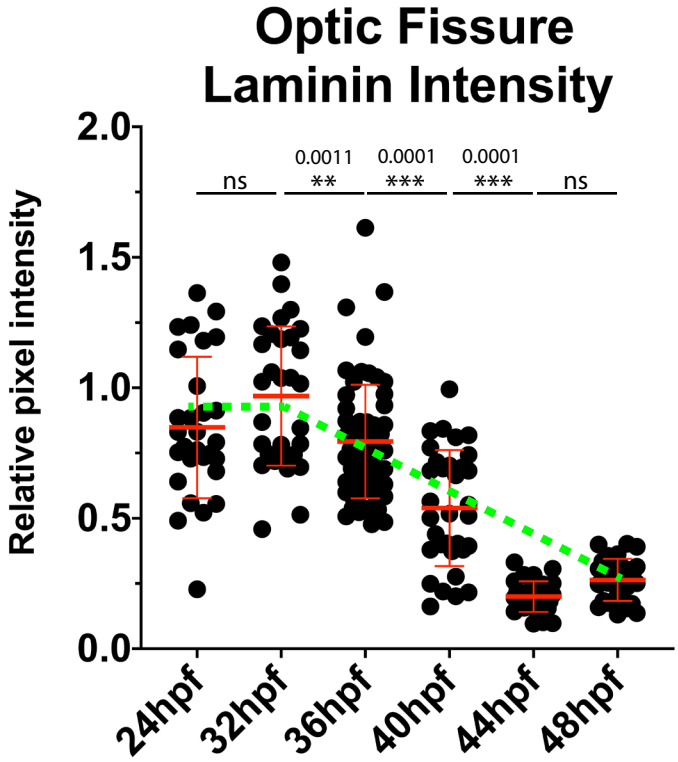
Optic Fissure
Laminin Intensity
Relative pixel intensity
2.0
1.5
1.0
0.5
0.0
ns
0.0011
**
0.0001
***
0.0001
***
ns
24hpf
32hpf
36hpf
40hpf
44hpf
48hpf

C

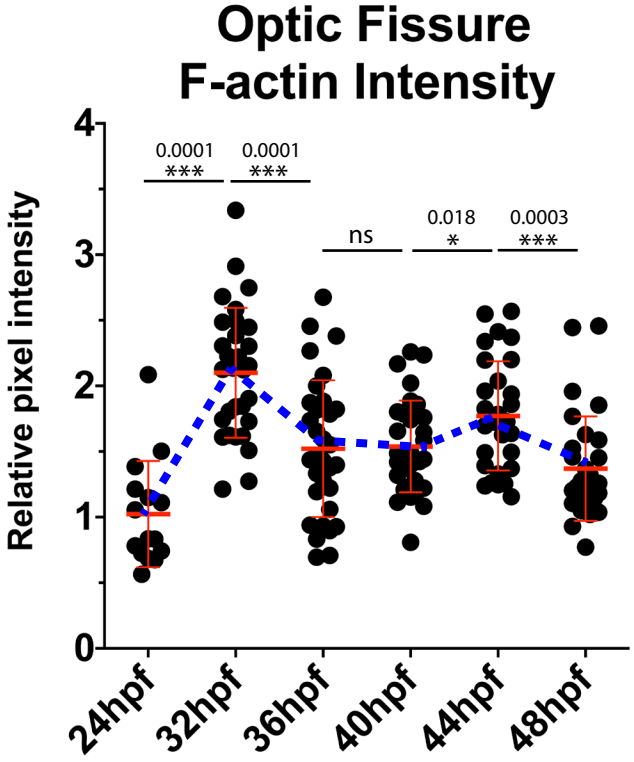
Optic Fissure
F-actin Intensity
Relative pixel intensity
4
3
2
1
0
0.0001
***
0.0001
***
ns
0.018
*
0.0003
***
24hpf
32hpf
36hpf
40hpf
44hpf
48hpf

Figure 2

A

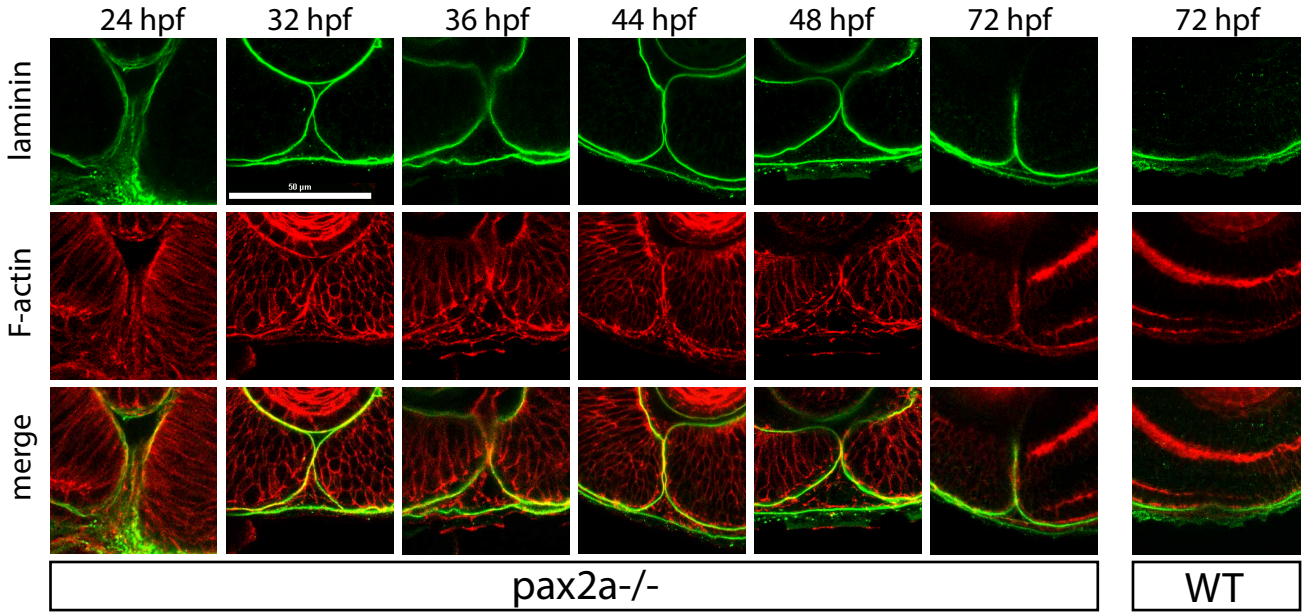
24 hpf
32 hpf
36 hpf
44 hpf
48 hpf
72 hpf
72 hpf
laminin
F-actin
merge
pax2a-/-
WT

B

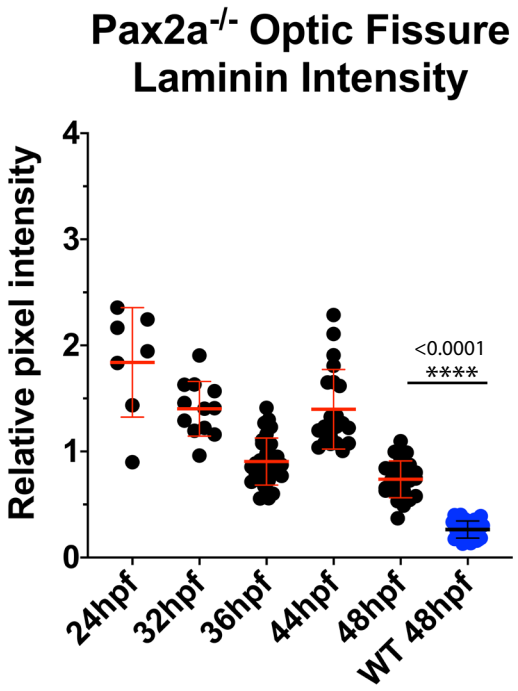
Pax2a-/- Optic Fissure
Laminin Intensity
Relative pixel intensity
0
1
2
3
4
<0.0001
****
24hpf
32hpf
36hpf
44hpf
48hpf
WT 48hpf

C

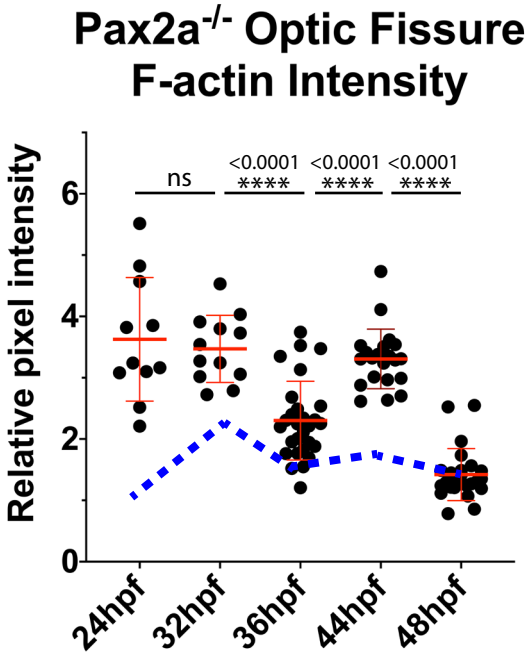
Pax2a-/- Optic Fissure
F-actin Intensity
Relative pixel intensity
0
2
4
6
ns
<0.0001
****
<0.0001
****
<0.0001
****
24hpf
32hpf
36hpf
44hpf
48hpf

Figure 3

A

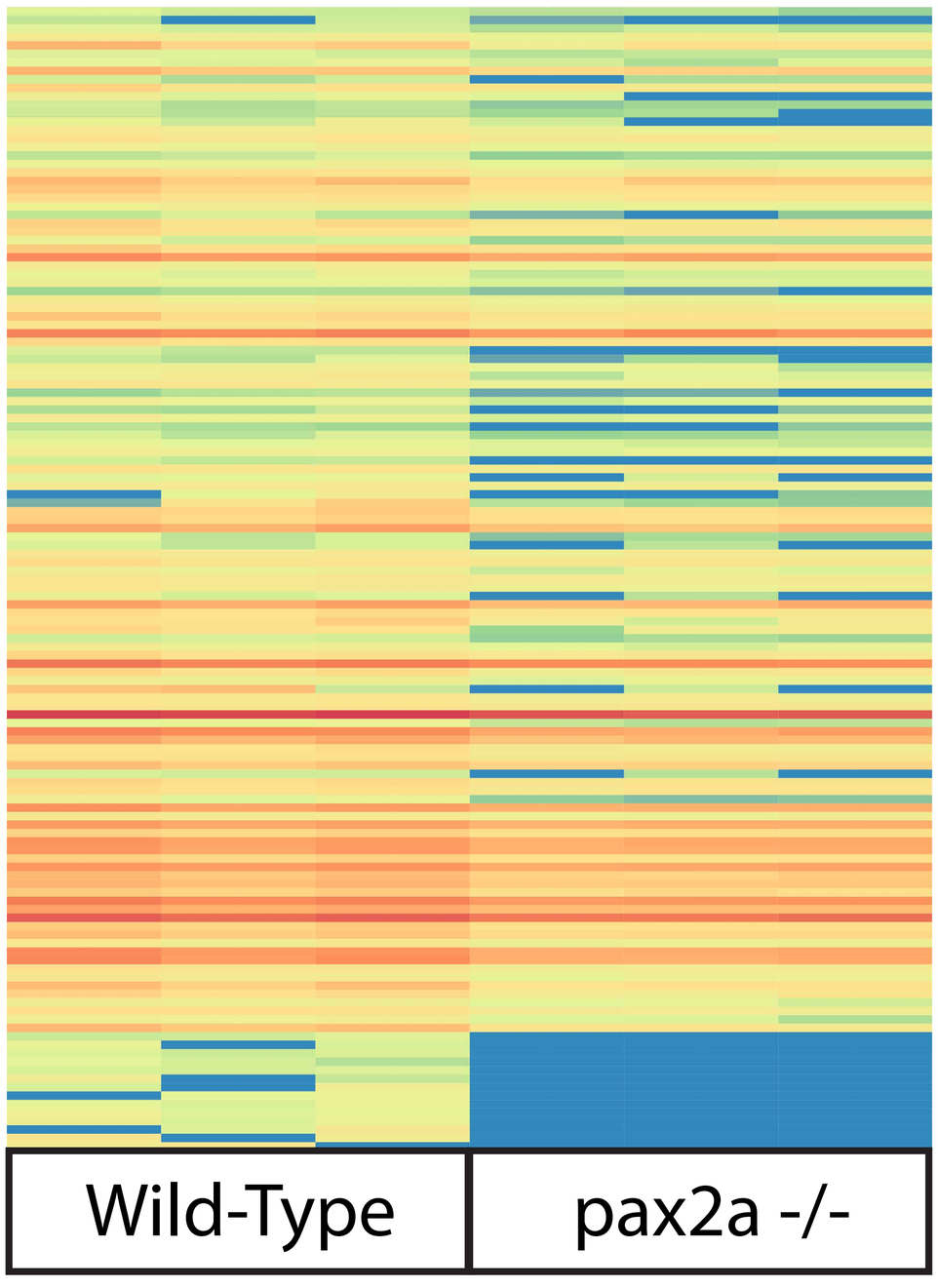

B

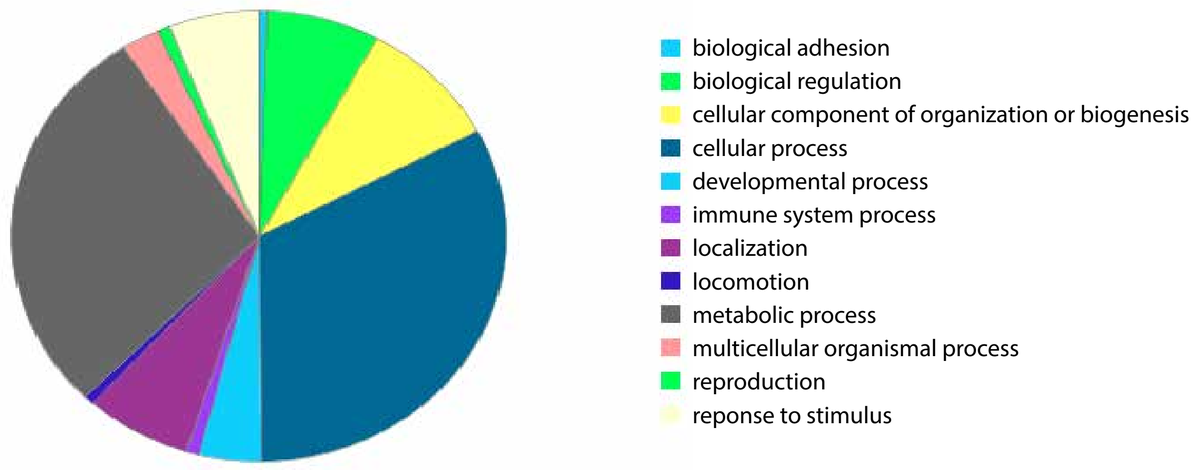

C

Gene ID	Gene Name	GO Term
aifm1	Apoptosis-inducing factor, mitochondrion-associated 1	oxidoreductase activity
sumo3a	small ubiquitin-like modifier 3a	protein sumoylation
lim2.1	Lens intrinsic membrane protein 2.1	Membrane
tfb2m	transcription factor B2, mitochondrial	transferase activity
tln1	Talin 1	actin binding
mgst2	microsomal glutathione S-transferase 2	enzyme activator activity
si:ch211-57b15.1	si:ch211-57b15.1	NA
ptprna	protein tyrosine phosphatase, receptor type, Na	protein dephosphorylation
dnajb11	DnaJ (Hsp40) homolog, subfamily B, member 11	protein folding
krt96	Keratin 96	structural molecule activity
sept9a	septin 9a	GTP binding
si:rp71-36a1.5	si:rp71-36a1.5	membrane
si:dkey-9c18.3	si:dkey-9c18.3	NA
arf5	ADP Ribosylation Factor 5	GTP binding
dock1	Dedicator Of Cytokinesis 1	small GTPase mediated signal transduction
hbbe1.1	Embryonic 1 beta-globin	Hemoglobin Complex
zgc:152951	Zgc:152951	electron transfer activity
pcbp3	Poly(rC)-binding protein 3	RNA binding
gpsm1b	G protein-signaling modulator 1b	GTPase regulator activity
abracl	Costars family protein ABRACL	regulation of actin filament-based process

D

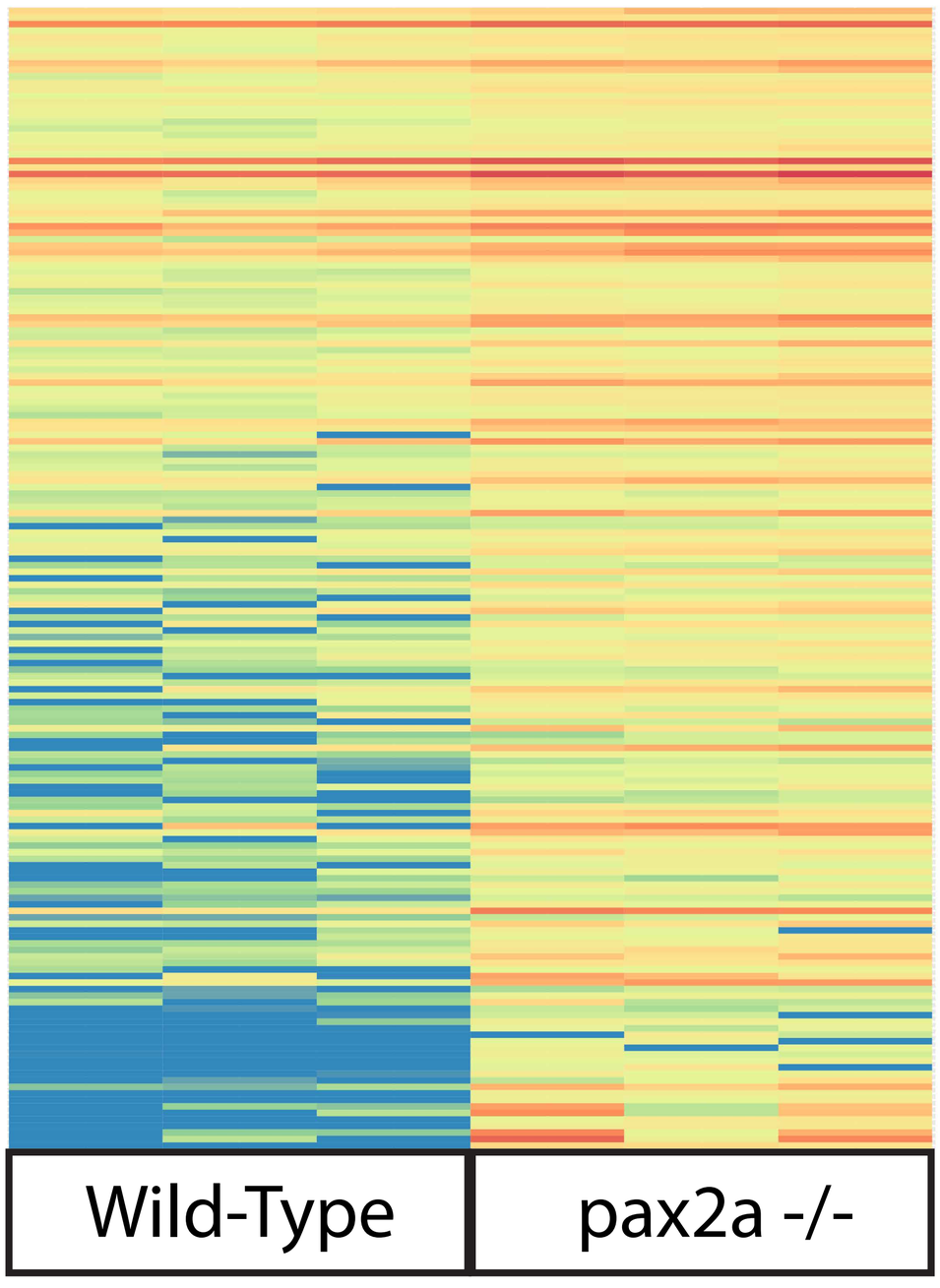

E

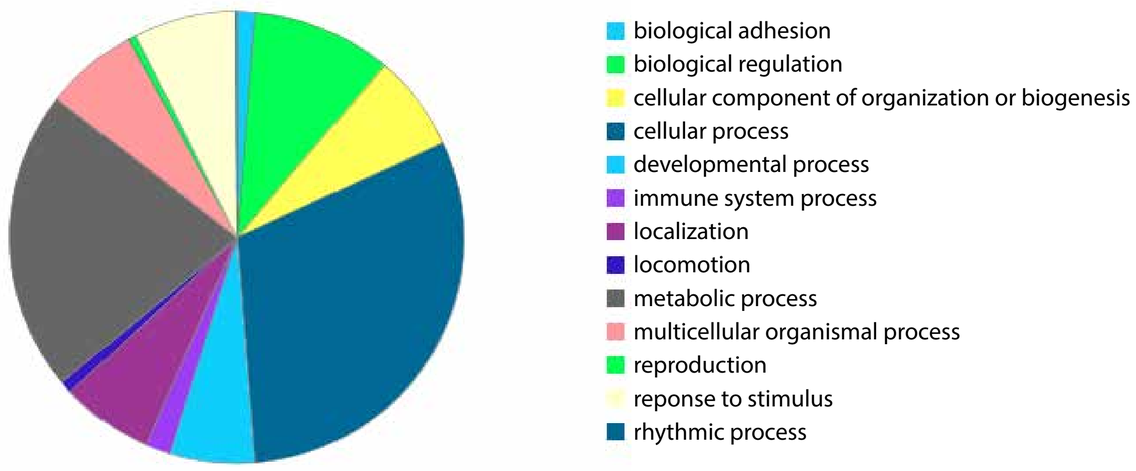

F

Gene ID	Gene Name	GO Term
gmnn	geminin, DNA replication inhibitor	regulation of DNA replication
col11a1a	collagen, type XI, alpha 1a	extracellular matrix structural constituent
fubp3	far upstream element (FUSE) binding protein 3	RNA binding
si:dkey-26g8.4	Cathepsin Lb	proteolysis
ublcp1	ubiquitin-like domain containing CTD phosphatase 1	protein dephosphorylation
smarcal1	SWI/SNF related, matrix, actin dependent regulator of chromatin, a-like 1	DNA repair
he1b	hatching enzyme 1b	metalloendopeptidase activity
anxa3a	annexin A3a	regulation of NMDA receptor activity
si:dkey-269i1.4	cathepsin L1-like	proteolysis
zgc:174855	zgc:174855	
gsta.1	glutathione S-transferase, alpha tandem duplicate 1	glutathione metabolic process
tbc1d7	TBC1 domain family, member 7	activation of GTPase activity
srek1	splicing regulatory glutamine/lysine-rich protein 1	regulation of alternative mRNA splicing
scg5	secretogranin V	neuropeptide signaling pathway
ggact.3	gamma-glutamylamine cyclotransferase, tandem duplicate 3	lyase activity
si:dkey-26g8.4	Cathepsin L1-like	proteolysis
si:dkey-239j18.3	si:dkey-239j18.3	proteolysis
ahsa1a	AHA1, activator of heat shock protein ATPase homolog 1a	ATPase activator activity
he1a	hatching enzyme 1a	metalloendopeptidase activity
dpf3	D4, zinc and double PHD fingers, family 3	zinc ion binding

Figure 4

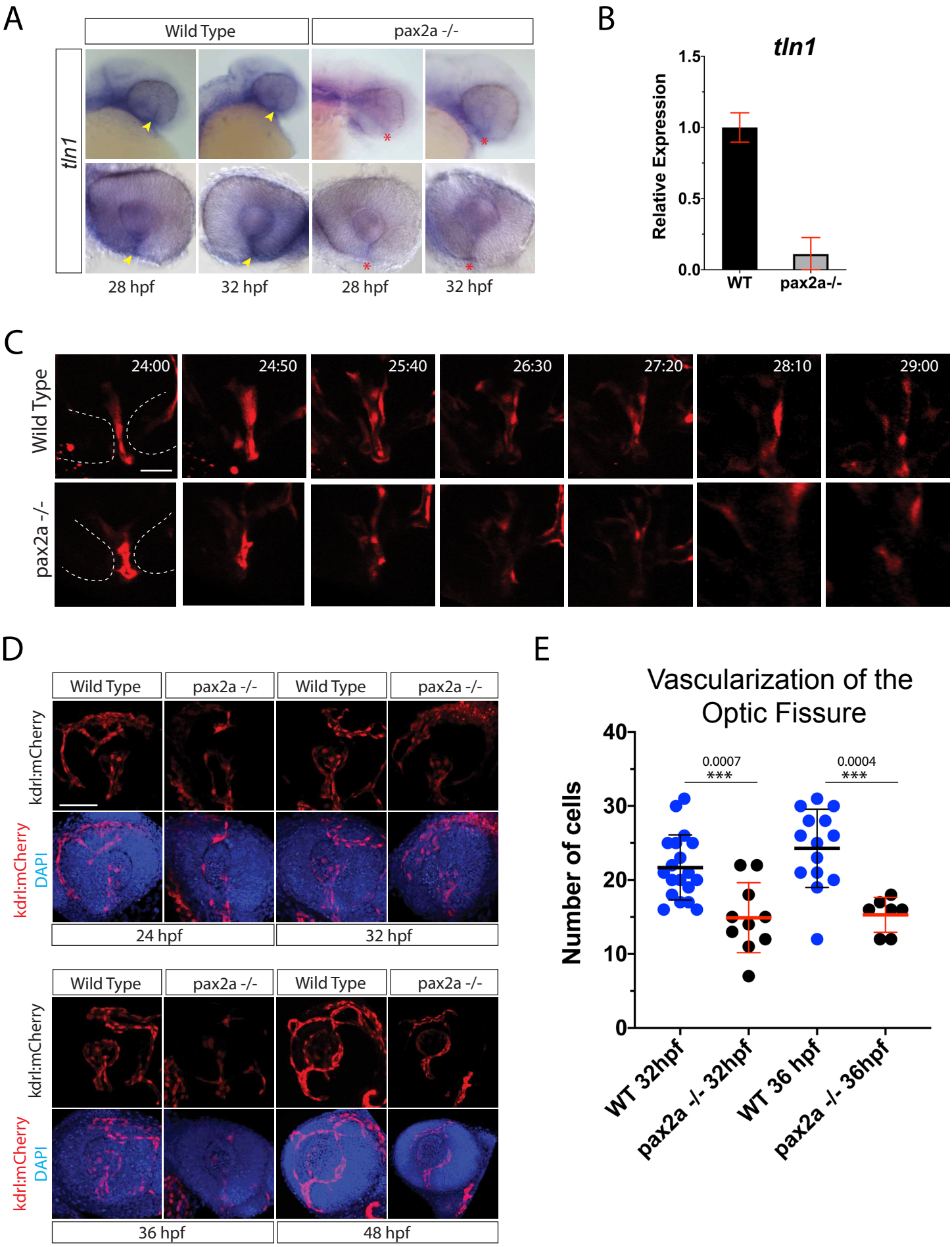
A
Wild Type
pax2a -/-
tln1
28 hpf
32 hpf
28 hpf
32 hpf
B
tln1
Relative Expression
1.5
1.0
0.5
0.0
WT
pax2a-/-
C
Wild Type
pax2a -/-
24:00
24:50
25:40
26:30
27:20
28:10
29:00
D
Wild Type
pax2a -/-
Wild Type
pax2a -/-
kdrl:mCherry
kdrl:mCherry
DAPI
24 hpf
32 hpf
Wild Type
pax2a -/-
Wild Type
pax2a -/-
kdrl:mCherry
kdrl:mCherry
DAPI
36 hpf
48 hpf
E
Vascularization of the Optic Fissure
Number of cells
40
30
20
10
0
0.0007
***
0.0004
***
WT 32hpf
pax2a -/- 32hpf
WT 36 hpf
pax2a -/- 36hpf

Figure 5

A

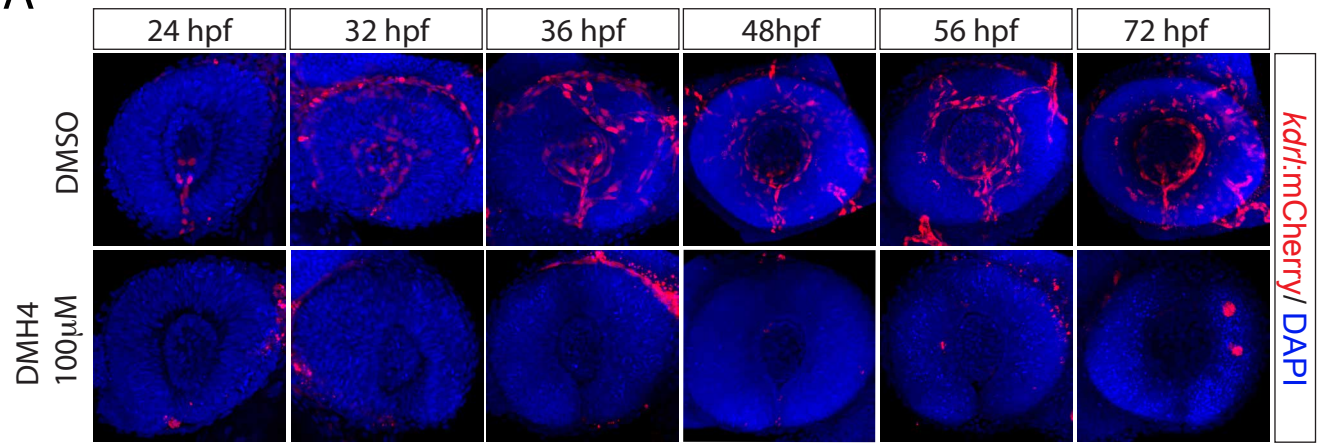

B

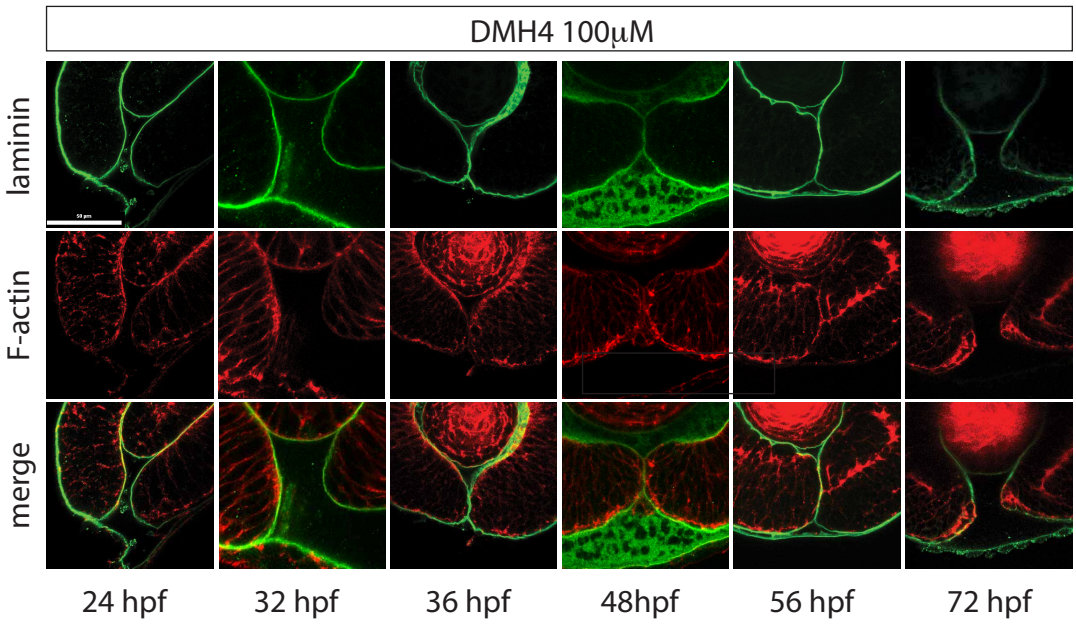

C

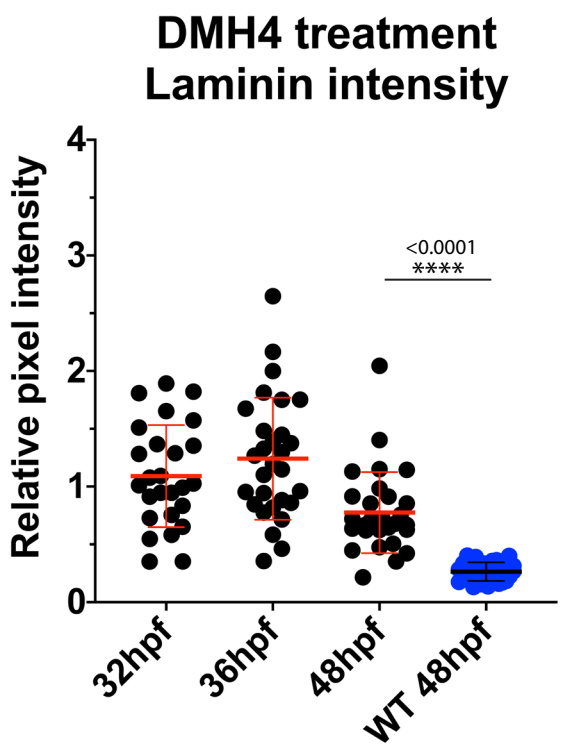

D

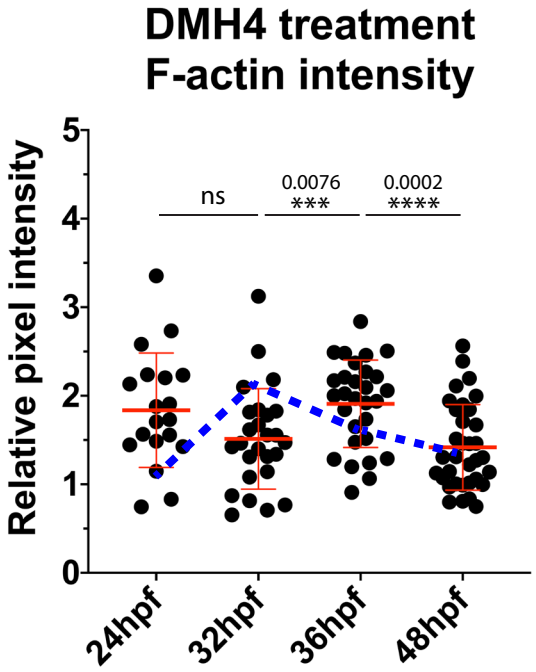

Figure 6

A

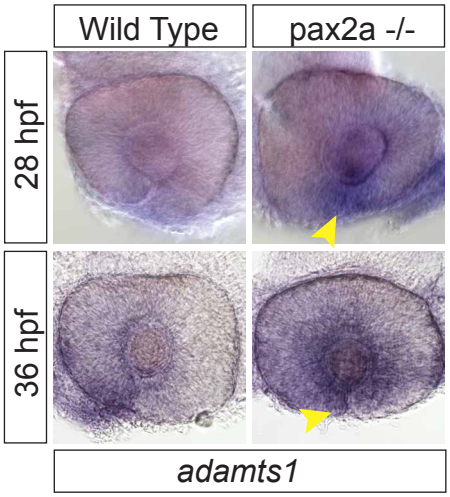

B

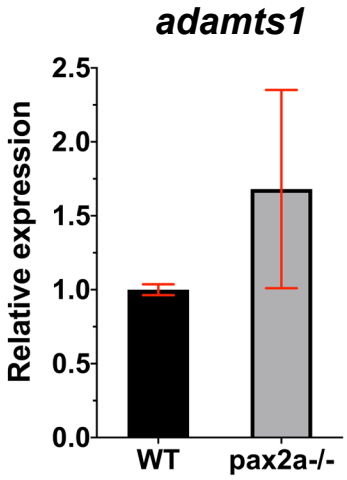

C

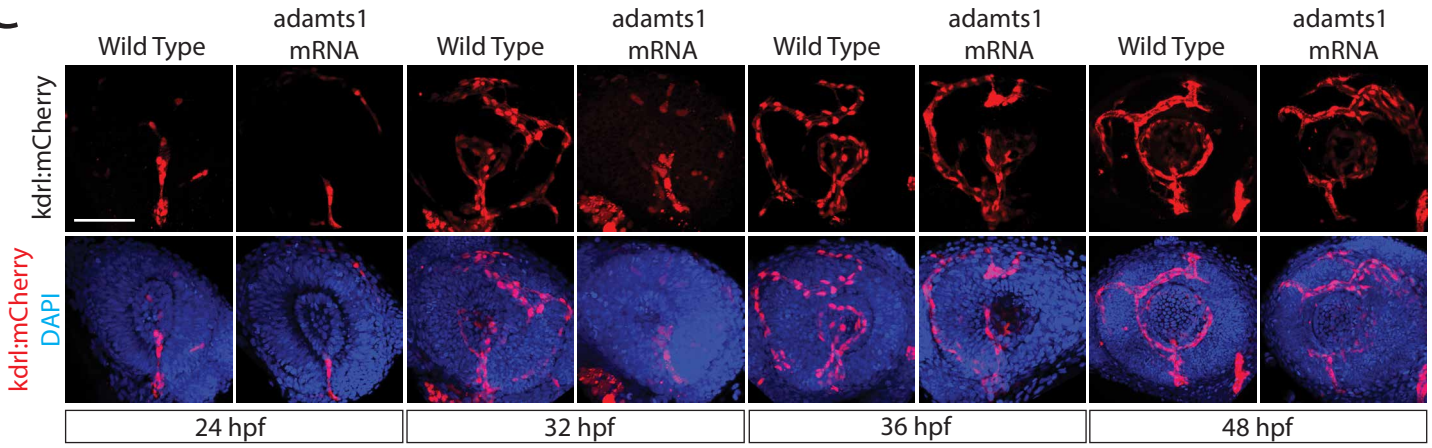

D

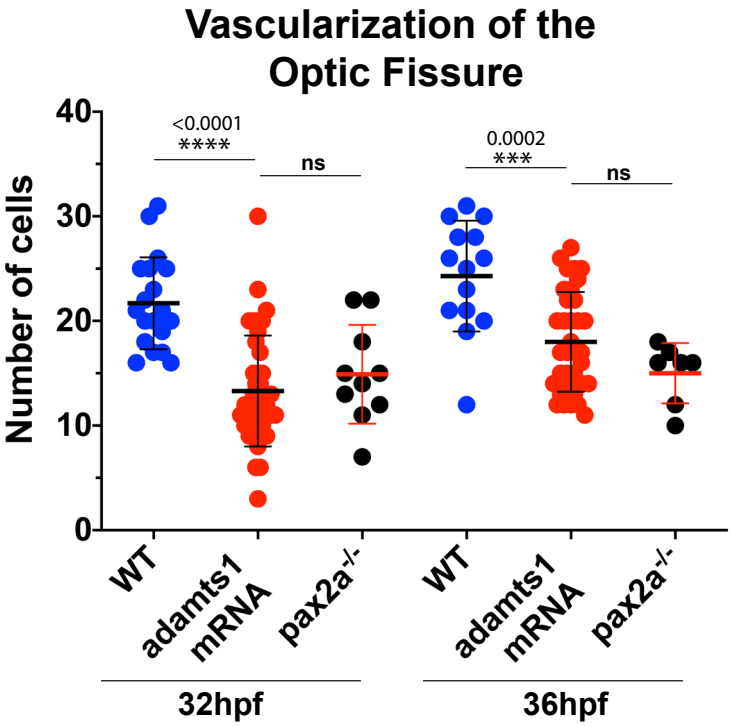

Figure 7

A

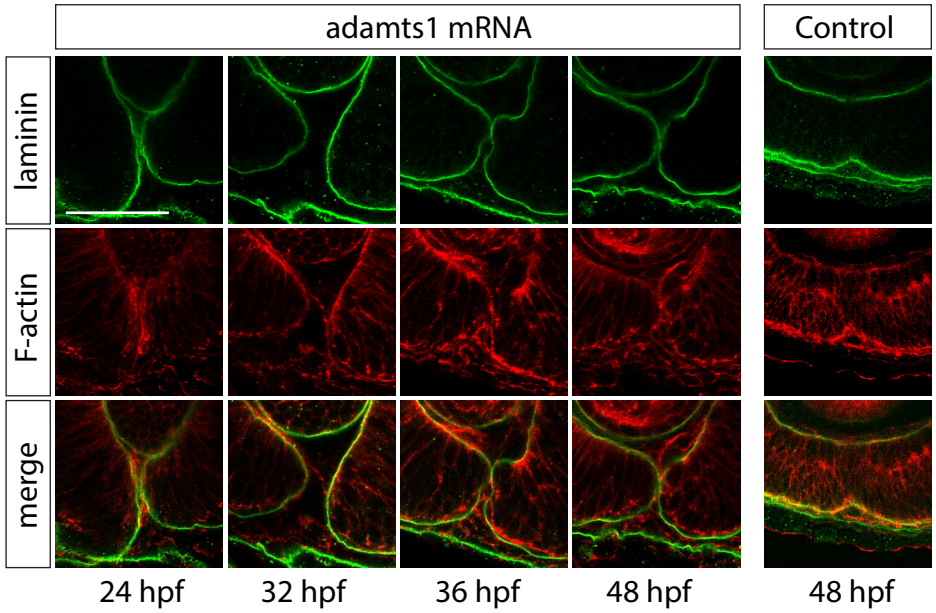
adamts1 mRNA
Control
laminin
F-actin
merge
24 hpf
32 hpf
36 hpf
48 hpf
48 hpf

B

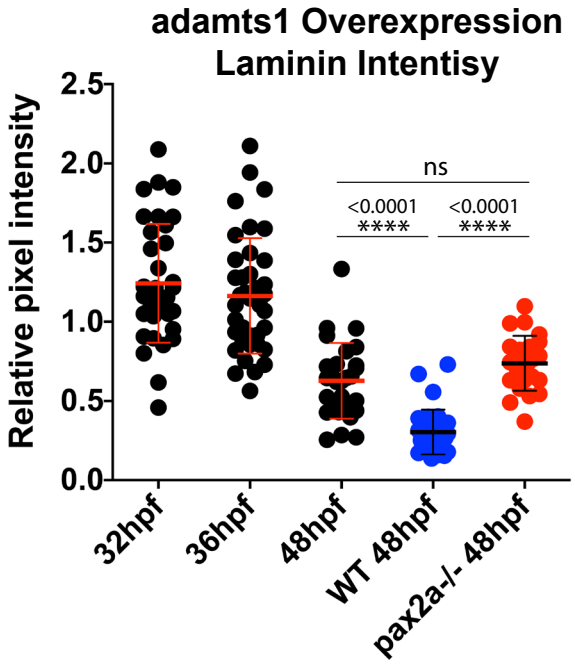
adamts1 Overexpression
Laminin Intentisy
Relative pixel intensity
2.5
2.0
1.5
1.0
0.5
0.0
ns
<0.0001
****
<0.0001
****
32hpf
36hpf
48hpf
WT 48hpf
pax2a-/- 48hpf

C

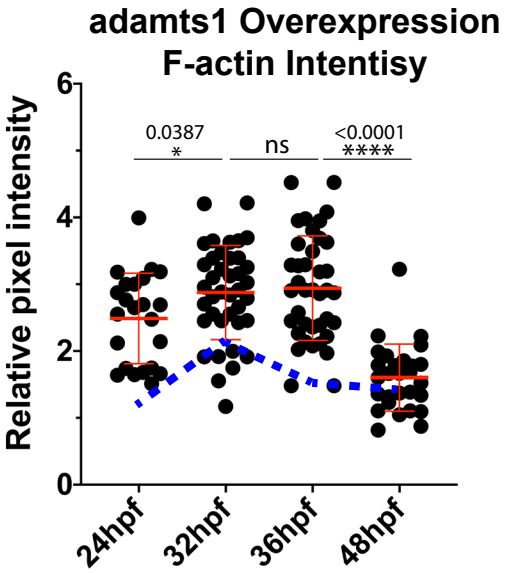
adamts1 Overexpression
F-actin Intentisy
Relative pixel intensity
6
4
2
0
0.0387
*
ns
<0.0001
****
24hpf
32hpf
36hpf
48hpf

Figure 8

A

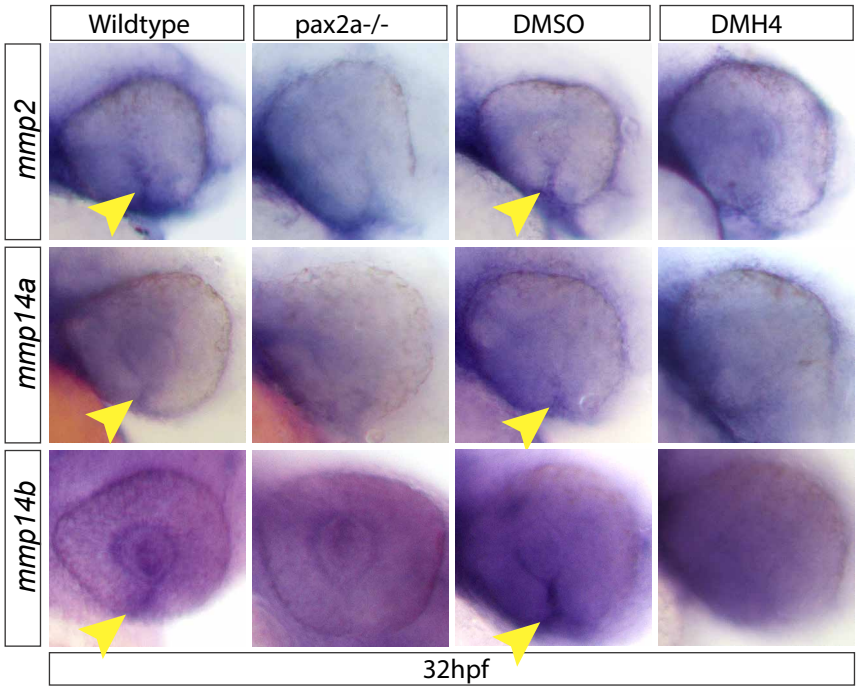

B

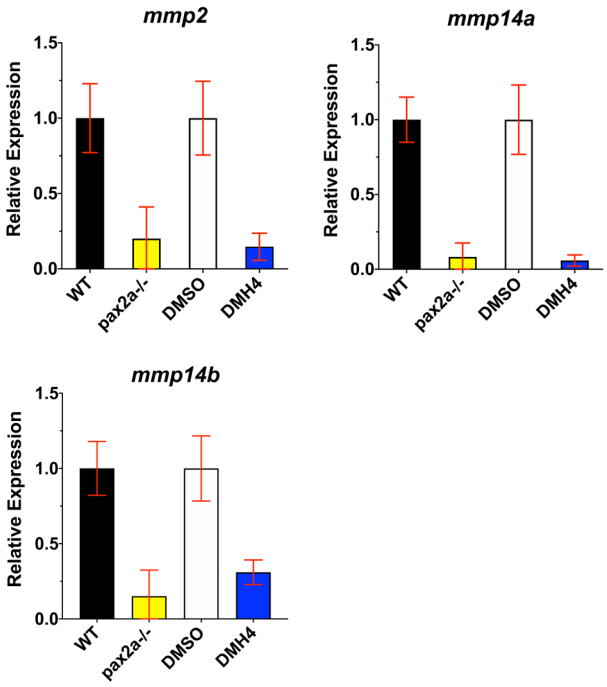

C

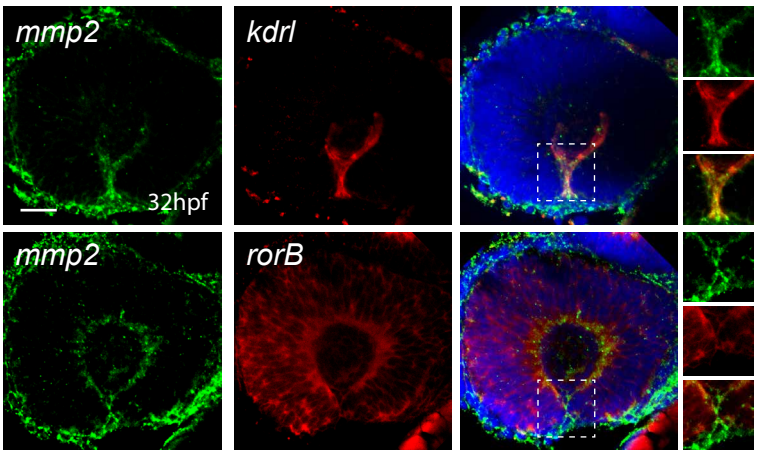

D

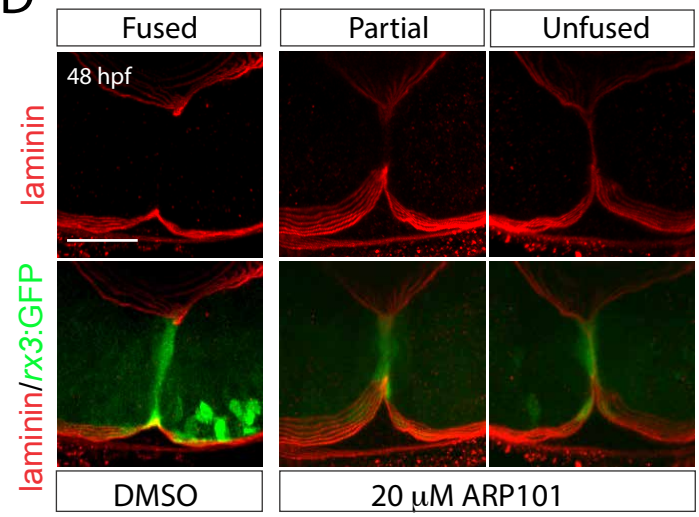

E

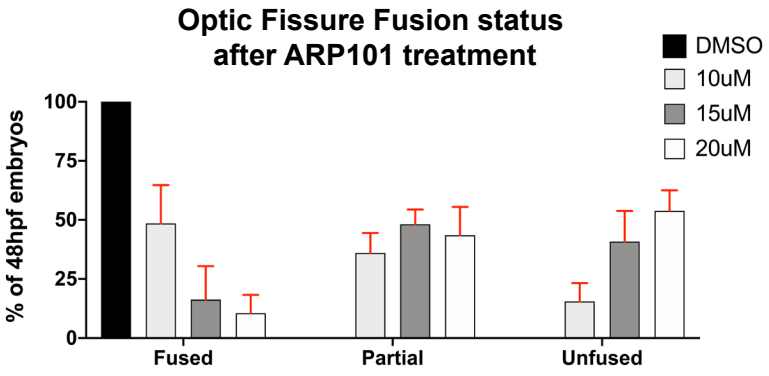

F

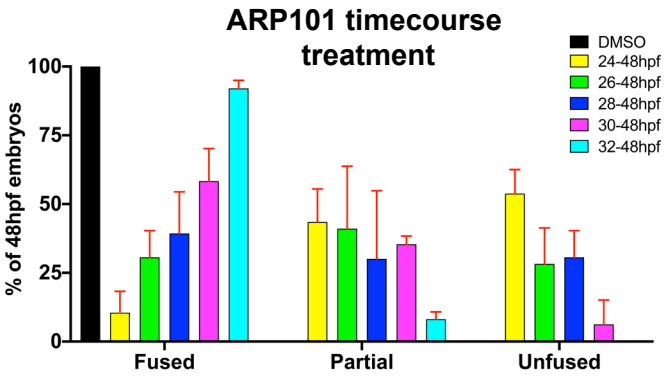

Supplementary Figure 1

A

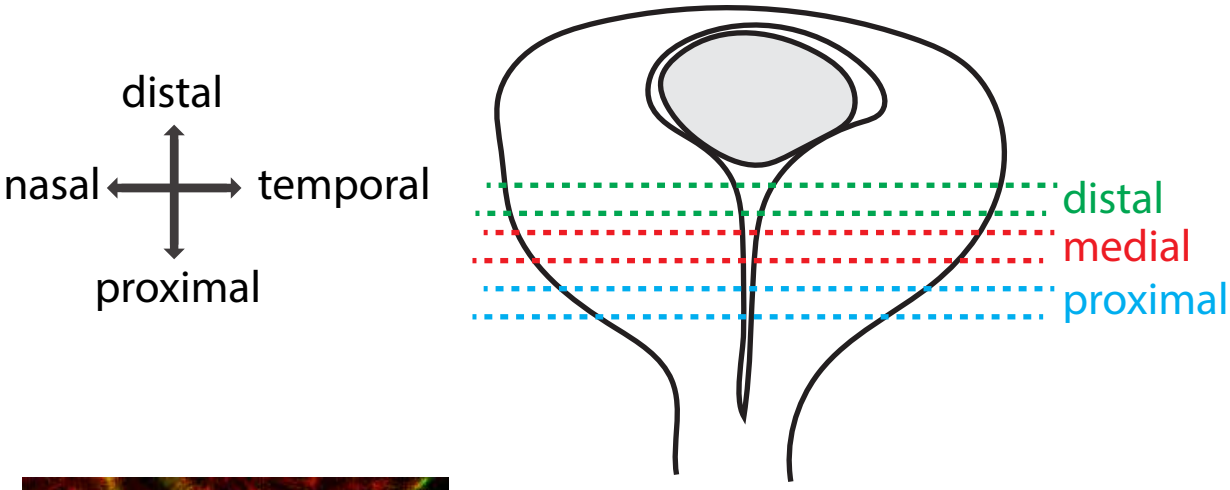

B

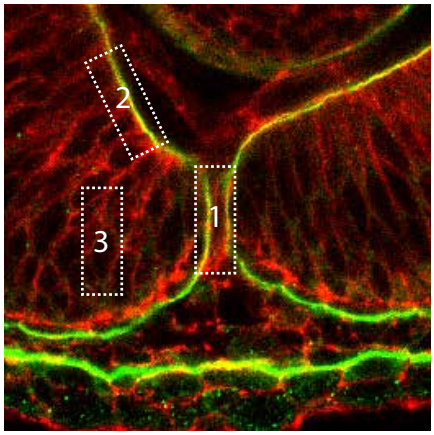

1: Optic Fissure Signal

2: Laminin signal normalization

3: Phalloidin (F-actin) signal normalization

C

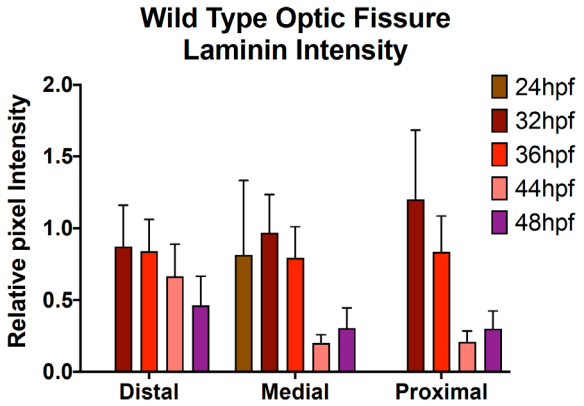

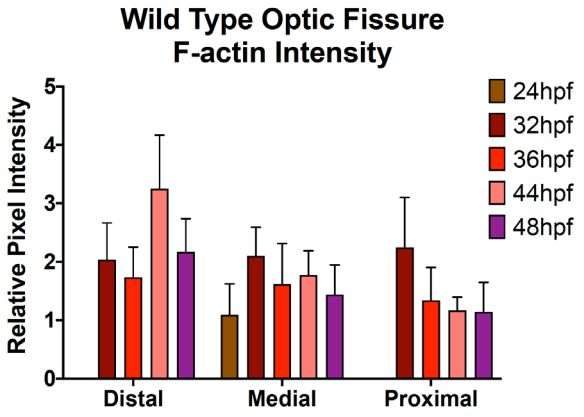

D

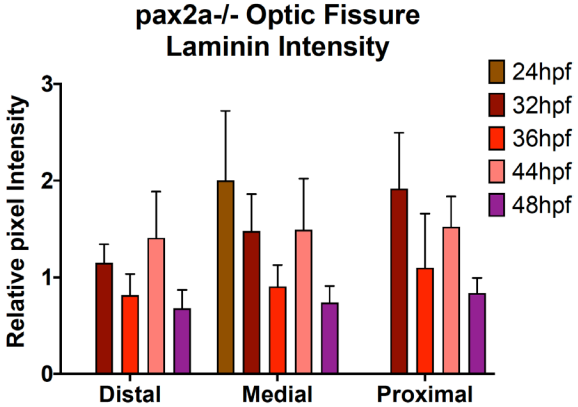

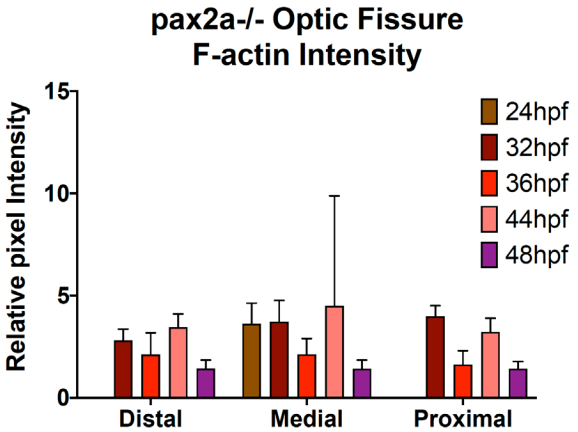

Supplementary figure 2

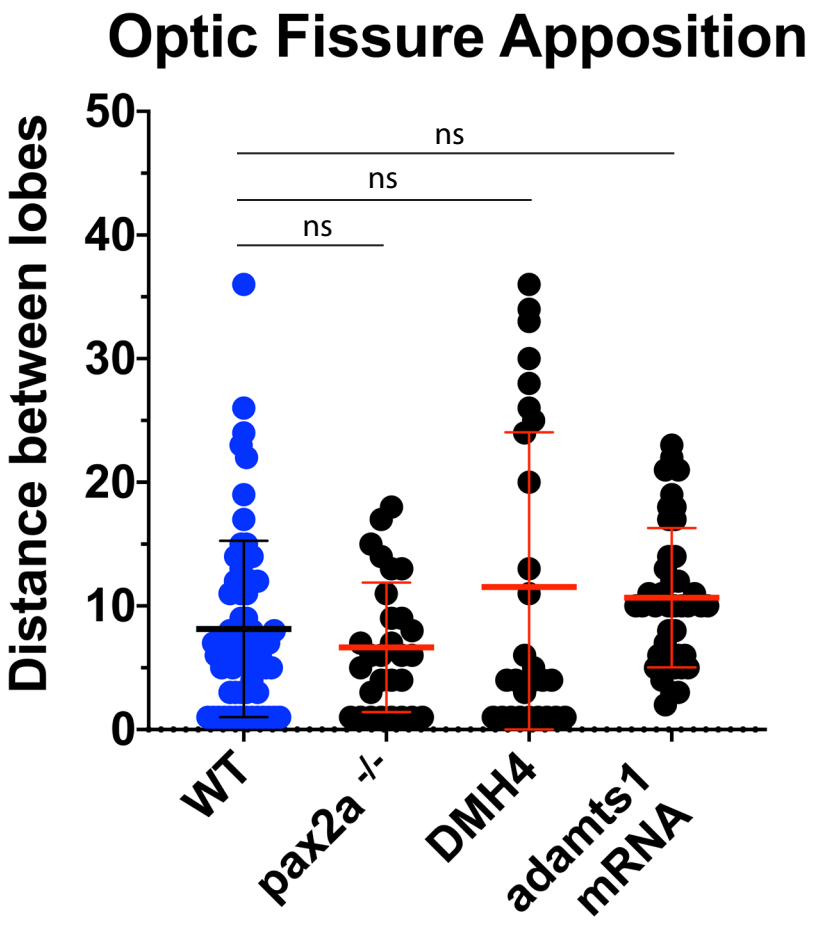

Supplementary Figure 3

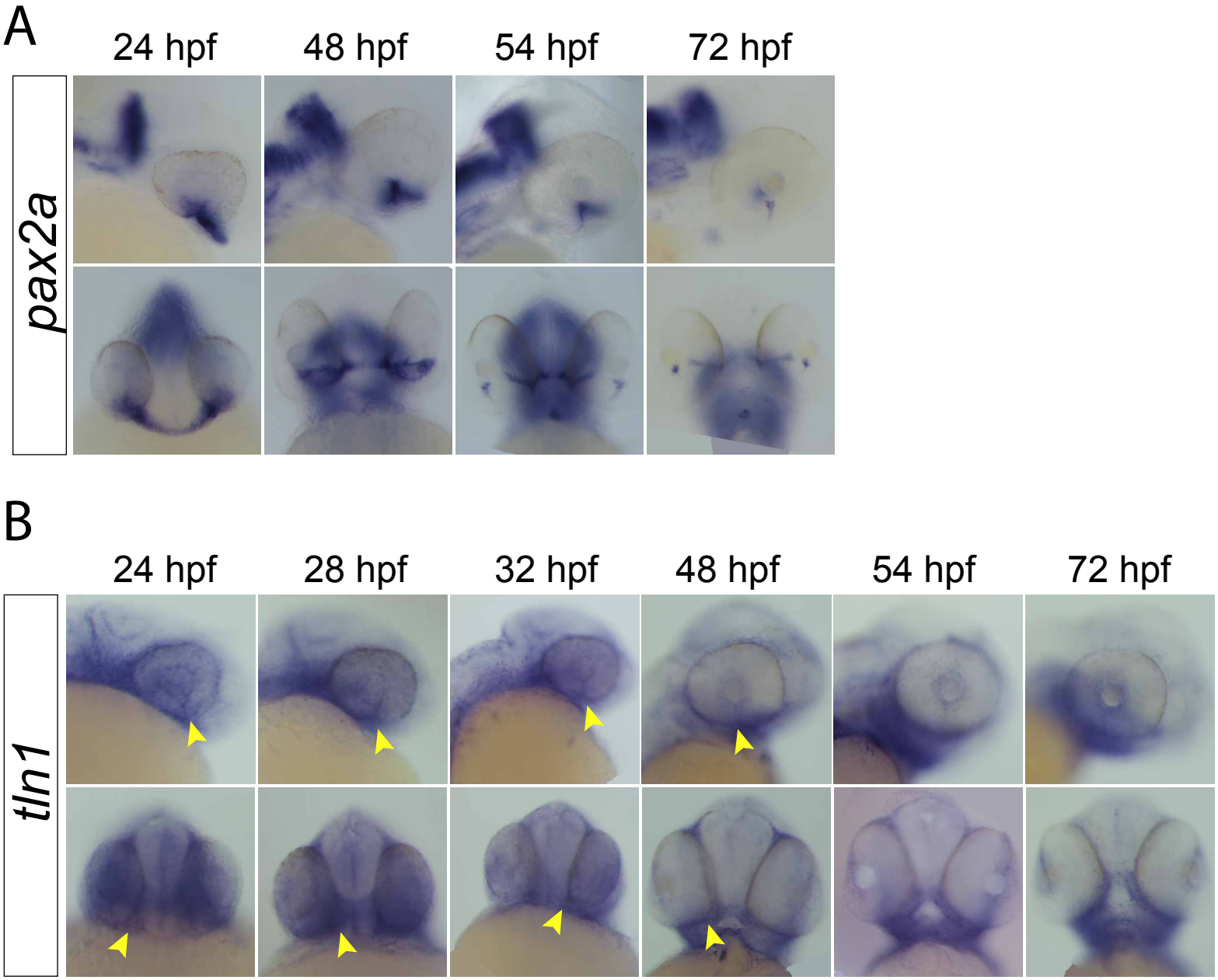

Supplementary Figure 4

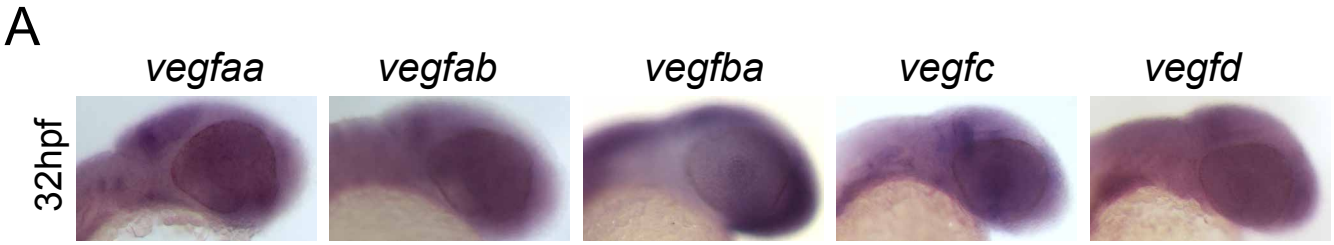

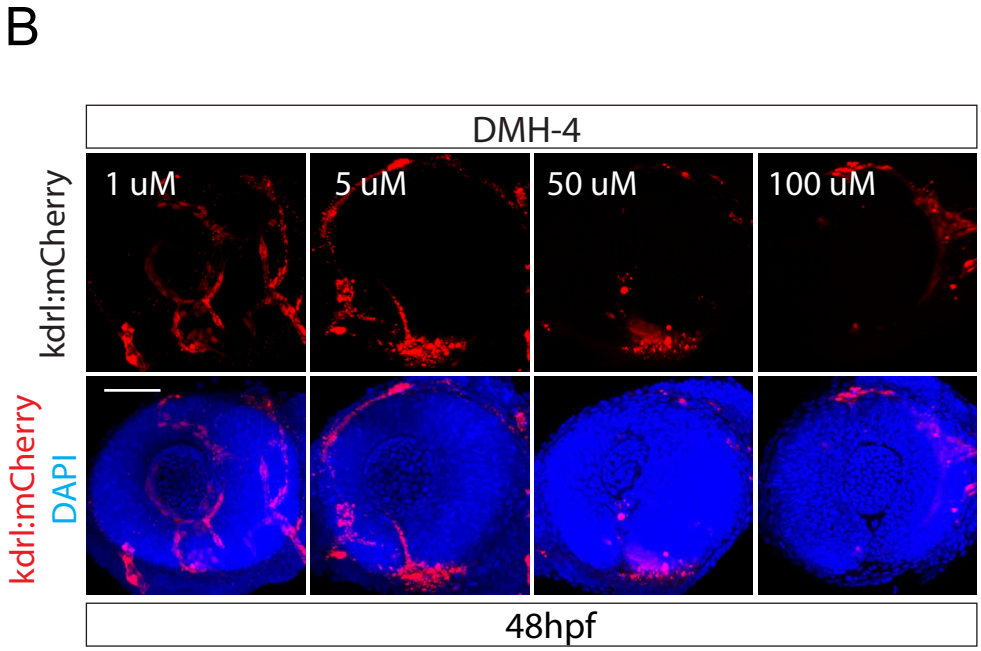

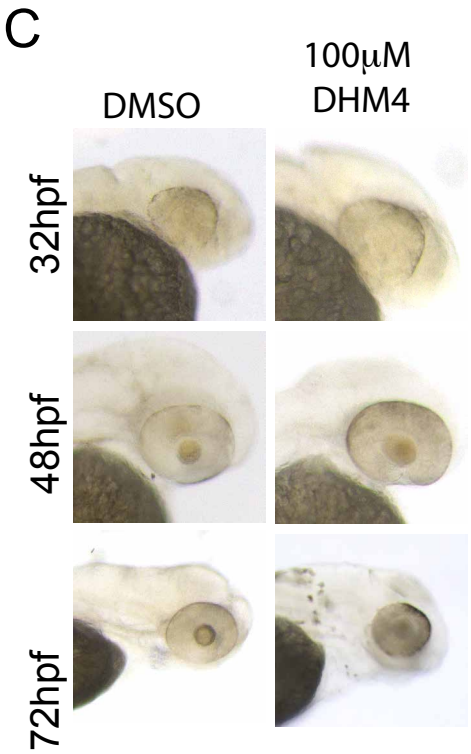

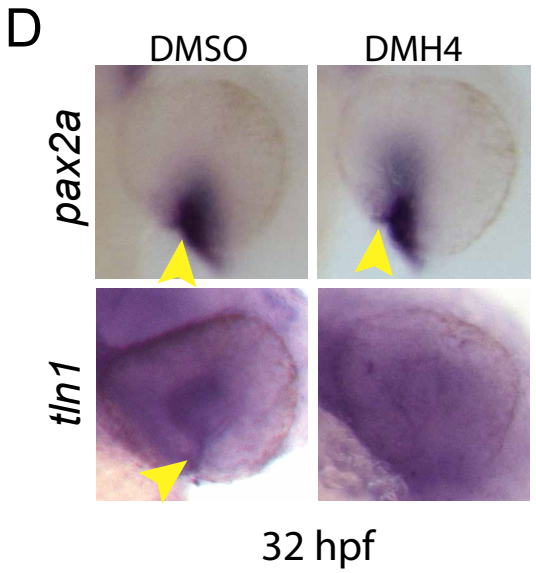

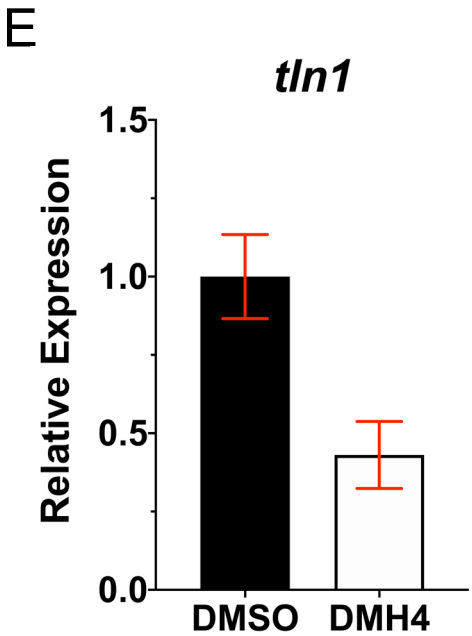

Supplementary Figure 5

A

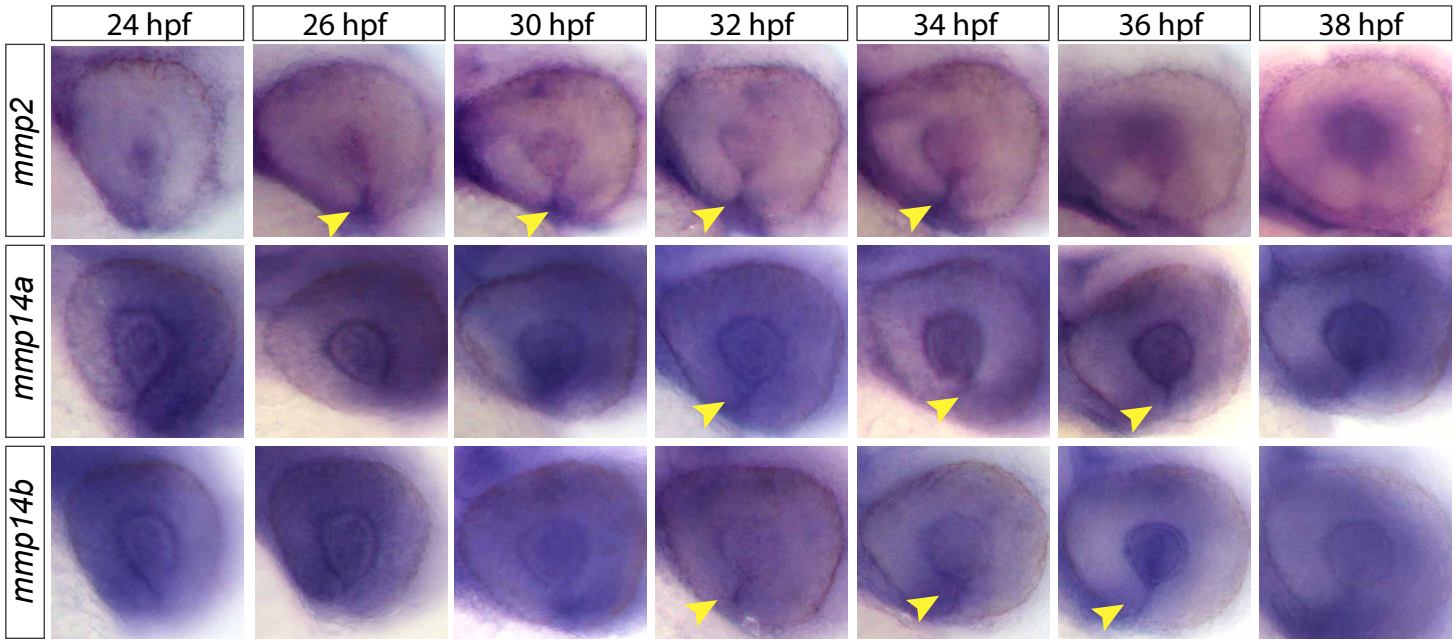
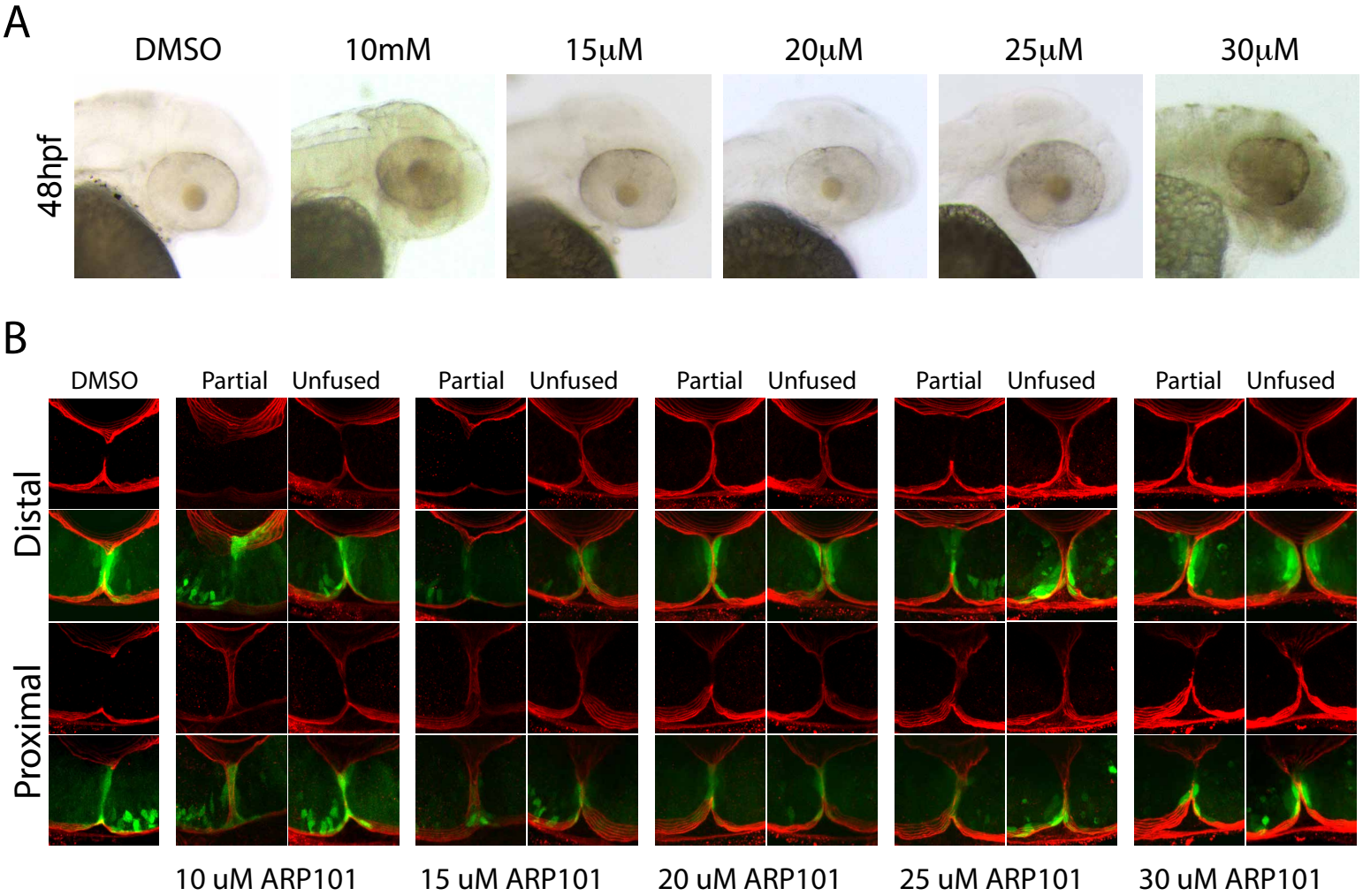
Supplementary Figure 6